1 **ELEVATION MODELING AND PALAEO-ENVIRONMENTAL INTERPRETATION IN THE SIWA AREA (EGYPT):**

2 **APPLICATION OF SAR INTERFEROMETRY AND RADARGRAMMETRY TO COSMO-SKYMED IMAGERY**

3 Riccardo Salvini[a*], Luigi Carmignani[a], Mirko Francioni[b], Paolo Casazza[a]

4

5 [a] University of Siena, Department of Environment, Earth and Physical Sciences and Centre of

6 Geotechnologies CGT. Via Vetri Vecchi 34, 52027, San Giovanni Valdarno (AR) Italy. Tel. +39 055 9119441,

7 e-mail: riccardo.salvini@unisi.it ([*]corresponding author), luigi.carmignani@unisi.it; paocasazza@gmail.com

8 [b] Department of Earth Sciences, Simon Fraser University, 8888 University Drive, Burnaby BC Canada, V5A

9 1S6. Tel. 778-782 6670, e-mail: mfrancio@sfu.ca

10

11 **ABSTRACT**

12 Digital elevation models produced from COSMO-SkyMed imagery were used to delineate palaeo-drainage

13 in a wide area surrounding the Siwa and Al-Jaghbub oases of the western Sahara Desert (Egypt and Libya).

14 This new generation of synthetic aperture radar imagery is suitable for this purpose because of its high

15 spatial resolution and capacity to penetrate dry surface sediments. Different techniques such as radar

16 interferometry and radargrammetry were used to produce digital elevation models. These were assessed

17 for accuracy and then combined to produce a single elevation model of the area.

18 The resulting elevation model was used to support the geological study and palaeo-environmental

19 interpretation of the area. It revealed buried features of the landscape, including inactive palaeo-drainage

20 systems. Drainage features were extracted from the elevation model using geographical information

21 systems; results were combined and assessed with respect to geological field data, as well as data from the

22 literature. Previous studies in the area suggest that a wide river, probably the old Nile River, flowed into the

23 Libyan palaeo-Sirte before the Late Messinian drawdown of the Mediterranean Sea. During the Late

24 Messinian lowering of the sea the fluvial system changed shape and carved deep canyons throughout

25 north-eastern Africa.

26 The reported findings on the key Siwa area were used to precisely delineate the physiography of the

27 modern drainage network and to confirm findings from our previous geological research in the area.

1 – INTRODUCTION

Research, conducted in the framework of the Italian Spatial Agency (ASI) "Announcement of Opportunity" project (Id: 2262), investigated the applicability of high resolution Synthetic Aperture Radar (SAR) imagery for the geological interpretation of drainage systems in an area between the Siwa (Egypt) and Al-Jaghbub (Libya) oases (Fig. 1). The area lies in the Libyan Calansho Desert, between the Qattara Depression and the Egyptian Western Desert, nearly 50 km east of the Libyan border and 560 km from Cairo. About 80 km long and 20 km wide, the study area is located in a deep depression up to -19 m below sea level. Both the Al-Jaghbub area, to the west, and the large Qattara Depression, to the east, lie below sea level.

In this work we investigated the integration of high spatial resolution images, such as those from the COSMO-SkyMed constellation, with the radar beam's ability to penetrate physically homogeneous, fine-grained land surface covers (Schaber et al., 1997). Such remote sensing imagery can provide information on subsurface features not detected by other passive sensors, and are therefore essential for delineating palaeo-morphological settings. In particular, X-band radar waves can theoretically penetrate dry sand to depths of approximately 30 cm without significant attenuation (Schaber et al., 1997). Remotely sensed data is also an important tool for scientists in such poorly accessible areas devoid of roads; moreover, data is easily interpreted due to the lack of vegetation.

This methodology was used to support previous studies on the geology and palaeo-morphology of the area carried out by the Siena University research group (Carmignani et al., 2009). The sand cover in the study area is relatively thin because the area lies on the edge of the Sahara Desert; recent analyses were based on fieldwork, micropaleontological data, and the photointerpretation of passive optical imagery such as Landsat ETM+ and Google Earth[TM], as well as Digital Elevation Models (DEM) derived from Advanced

55 Spaceborne Thermal Emission and Reflection Radiometer (ASTER) and Shuttle Radar Topographic Mission

56 (SRTM) data.

57 Several studies (McCauley et al., 1986; Robinson et al., 2006; Paillou et al., 2009) have made use of radar

58 imagery to investigate palaeo-channels buried under the sand cover. Radar mapping of subsurface features

59 gained wide attention in the early '80s thanks to the success of the National Aeronautics and Space

60 Administration's Shuttle Imaging Radar Mission (NASA SIR-A), which revealed channels buried under the

61 sands of the Sahara Desert (McCauley et al., 1982).

62 Different techniques such as interferometry and radargrammetry were used in this study to create DEMs

63 from COSMO-SkyMed active remote sensing data. Since both methodologies have their peculiarities,

64 advantages and limitations, they were combined in order to obtain a final elevation model with the best

65 possible accuracy compared to GPS data from fieldwork and from a reference DEM. To this end, in the

66 absence of elevation models based on either aerial LIDAR (LIght Detection And Ranging) or aerial photos, a

67 DEM derived from SRTM data was selected as reference. SRTM data have yielded interesting results in

68 previous studies of areas with similar environmental conditions (Ghoneim and El-Baz, 2007; Youssef, 2009).

69 New high spatial resolution DEMs have allowed even more detailed, accurate geomorphological analyses

70 than previous studies; in Carmignani et al. (2009) the study was accomplished by using DEMs with a lower

71 spatial resolution produced from SRTM and ASTER data (the latter from stereophotogrammetry of L1A

72 products).

73 DEMs generated from COSMO-SkyMed imagery were assessed for accuracy with the goal of checking their

74 reliability and, as a consequence, the correctness of interpretation and accuracy of performed spatial

75 analyses. GIS (Geographic Information System) spatial analysis was then used to automatically extract the

76 drainage network, allowing the identification of recent channels and the interpretative historical

77 reconstruction of possible palaeo-channels and palaeo-environments.

78

79

80 **2 - GEOLOGY AND GEOMORPHOLOGY**

81

The geological setting of the area was shaped by tectonic processes and, starting in the Paleozoic, by several transgression-regression cycles. Egypt belongs to the African Craton and is characterized by Paleozoic and more recent basins that were subsequently infilled and modified; the area is extremely stable and not affected by significant endogenous activity. The Miocene rocks, the most frequent in the Western Desert, lie disconformably above the older Precambrian to Oligocene deposits (Tawadros, 2001). National geological maps of Egypt and Libya at a 1:500,000 scale were used along with field data on Libya from the '70s and '80s (courtesy of Prof. Luigi Carmignani). The lithologies cropping out in the Siwa area mainly refer to two Miocene formations (Said, 1962; Abdel-Fattah et al., 2013): the *Marmarica* Formation, a fossiliferous shallow-marine carbonate sequence with a few marly intercalations, ascribed to the Middle Miocene, and the continental to shallow-marine clastic sequence of the *Moghra* Formation, dated to the Early Miocene (Fig. 2). The latter formation comprises shale and white sandy carbonate beds, abundant silicified woods, and the uppermost carbonate layers are transitional to the *Marmarica* Formation. East of the study area, the Middle Eocene is represented by the *Mokattam* Group, a transgressive-regressive sequence of neritic limestone with frequent echinoids, *Nummulites gizehensis*, *Nummulites leyelli* and *Nummulites zitteli* and with a white chalky neritic limestone at the base that is underlain by a neritic grey shale. South-east of Siwa, the Late Eocene is represented by the *Qasr el-Sagha* Formation, a littoral marine to continental clastic sequence with oyster beds and coquina layers; intercalations of silt- and claystone are also present. In lower parts, *Nummulites striatus* and *Nummulites fabiani* abound in fossiliferous calcarenite.

This geological setting was confirmed by the micropaleontological analysis of few rock samples collected during fieldwork with the aim of determining the depositional and sedimentary environment in which the lithologies formed. The rock samples were analyzed in collaboration with the Micropaleontology Laboratory of the Earth Sciences Department of *La Sapienza* University in Rome. The collected samples are ascribed to the Middle Miocene due to the presence of the *Neomonoceratinakeiji* species of *Neomonoceratina* (Szczechura and Abd-Elshafy, 1988). The stratotype is the *Marada* Formation, whereas the type locality is located in central Libya, south of the Sirte Basin, between the Marada and Dahra localities (Fig. 1). Analyses confirm the genesis of rocks in the North Western Desert reported in the

4

literature: they belong to the *Moghra* and *Marmarica* formations (Said, 1962), which can be referred

respectively to the lower and upper facies of the Middle Miocene *Marada* Formation in Libya (Tawadros,

2001). In the Sirte area, these facies are in turn correlated with the *Rajmah* Formation and the *Al-Jaghbub*

Formation (Carmignani et al., 1990). According to Abdel-Fattah et al. (2013) the *Moghra* and *Marmarica*

formations can be respectively dated to the Early Miocene (Aquitanian-Burdigalian) and the Middle

Miocene (Langhian-Serravallian). None of the Late Miocene and Pliocene sediments crop out in the

surroundings of the study area.

The Quaternary cover sediments are represented by *sabkha* (saline, puffy, crusted flat-bottomed basins

intersecting the water table and forming a kind of playa) deposits which, near lakes, are intercalated with

silt, clay and evaporites. The clastic sedimentary rocks present in the area result from fluvial and

gravitational processes within the valleys (locally called *Wadi*). All these sediments lie disconformably

above the Middle Miocene *Marmarica* Formation. *Wadi* is an Arabic term traditionally referring to a valley

with a dry (ephemeral) riverbed that contains water only during times of heavy rain or simply an

intermittent stream. South of the oases, wind erosion produced the currently expanding sand dunes of the

Calansho Desert.

The morphology of the area and of the entire Western Desert is the result of long, unceasing peneplanation

processes operating since the beginning of the Tertiary. This process has produced a remarkably uniform,

generally tabular and desertic landscape with high plateaus in the northern part of the study area and

lower ones to the south. The various geomorphic agents have worked together or in turn at different times,

producing peculiar morphologies such as the *garats*, small mesas or buttes formed in the Miocene rocks of

the area (Fig. 3). Former streams eroded the bedrock, leading to the formation of early *garats*. Wind action

and high temperatures subsequently shaped the present mesas and buttes.

Rivers and streams have modelled the landscape, in apparent contrast with the current arid climate

conditions and the almost complete absence of active drainage networks. Carmignani et al. (2009)

attempted to reconstruct past environmental conditions. They hypothesized that before the Late Messinian

drawdown of the Mediterranean Sea (Ryan and Cita, 1978) palaeo-Nile flowed from Asyut (Egypt – Fig. 1),

passing south of the Qattara Depression and proceeding in a west-northwest direction through the Siwa

5

and Al-Jaghbub oases, finally reaching the palaeo-gulf of Sirte (Fig. 4). This fluvial system consisted of shallow erosive channels (a few meters at most) in Libya and deeper ones at Siwa (up to some tens of meters). This palaeo-river was characterized by a delta that can still be seen in an area extending more than 100 km along the eastern margin of the palaeo-Sirte, as far as the Calansho Desert boundary (Carmignani et al., 2009).

Geological literature on the Sirte area (Carmignani et al., 1990) describes a second drainage system, represented by the canyons of the Late Messinian drawdown of the Mediterranean Sea, which are clearly visible on optical satellite images. In Libya this palaeo-drainage, which cut and sometimes captured the previous system, is covered by the Pliocene deposits of the *Qarat Weddah* Formation (Di Cesare et al., 1963). Its morphology, characterized by wide, flat-bottomed *wadis* with steep escarpments up to 50-60 m high, is different from that of the pre Late Messinian drawdown of the Mediterranean Sea. The second system can be traced westward from Qarat Weddah to the present Gulf of Sirte and eastward from Siwa to the present Nile Delta. Fig. 4 shows a schematic representation of this reconstruction.

3 – METHODS

The ASI dataset consists of 13 COSMO-SkyMed 2 and 3 tandem Hi-Image STRIPMAP products characterized by 1A SCS-B processing level, Hierarchical Data Format ver. 5 (HDF5) and 3x3 m ground range and azimuth resolution (ASI, 2009). The nominal footprint size is 40 x 40 km, and polarization is horizontal in both transmission and reception (HH). Images were acquired in both ascending and descending orbit configurations with different incidence angles: ranging from 15° to 20° for radargrammetric sets and from 30° to 40° for SAR interferometric sets.

SAR images are stored as Single Look Complex (SLC) files containing both amplitude and phase information on signals backscattered from the ground targets. The dataset was acquired from April to July 2011. The area covered by imagery extends from 24°35' east - 29°45' north and 25°35' east - 29°02' north. COSMO-

162   SkyMed (CSKM) images cover this area several times both in ascending and descending orbits: available

163   scenes were therefore divided into two subgroups named "Nile1" and "Nile2" (Fig. 5).

164   The first area (Nile1), to the east, covers a vast portion the Siwa Oasis comprising the lakes and the

165   numerous *garats* in the surrounding territory. The escarpment of the El-Diffa Plateau characterizes the

166   northern part of the Nile1 area, whereas the dunes of the Calansho Desert characterize the southern

167   landscape. Nile2 comprises the territory northwest of Siwa, including the western portion of the El-Diffa

168   Plateau escarpment, some of the ephemeral lakes east of the Al-Jaghbub Oasis, and the northern dunes of

169   the Calansho Desert. Fig. 6 shows two examples of footprint and quick look of CSKM descending scenes for

170   Nile1 and Nile2 areas.

171   As mentioned earlier, the study also made use of passive optical images such as Landsat ETM+ (path-row:

172   176-41, 176-42, 177-41) and Google Earth[TM], as well as ASTER and SRTM DEMs. The ASTER DEM, called G-

173   DEM, was derived from satellite imagery using photogrammetry; it has a nominal spatial resolution of 30 m.

174   The vertical accuracy of this DEM is about 20 m LE95 (Linear Error at 95% confidence). Data is referred to

175   the Spheroid WGS84 - Datum EGM96 (World Wide 15-minute Geoid Height) and is available in Geotiff

176   format. The SRTM DEM has a nominal spatial resolution of 90 m and its reported vertical accuracy is about

177   16 m LE90 (at 90% confidence). This DEM has a penetration capability, in dry sand environments, up to

178   depths of 50 cm (Ghoneim and El-Baz, 2007). Data is georeferenced to the WGS84/EGM96 system and is

179   available in Geotiff format. The SRTM DEM and G-DEM were reprojected from the EGM96 Datum to

180   WGS84 for use in interferometric and photogrammetric processing of CSKM images. The accuracy of the

181   reprojected DEMs was subsequently assessed using Ground Control Points (GCP) from the GPS survey

182   completed during fieldwork: differences were always less than 4 m with a standard deviation of 10 m.

183   The following paragraphs describe the interferometric and radargrammetric processing of SAR data used to

184   produce the DEMs that were subsequently validated and compared to those from the SRTM mission.

185

186

187   **3.1 - InSAR PROCESSING**

188

189 Interferometric SAR (InSAR) processing requires short temporal baselines between images in order to

190 ensure maximum coherence between acquisitions. Coherence may be expressed as a measure of the

191 similarity between the backscattered signal in the area of overlap between two SAR images; it consists of

192 an adimensional number ranging from 0 to 1. Starting from the available set of images and considering

193 different temporal and spatial baselines, two image pairs in right ascending configuration and two in right

194 descending configuration were acquired. Each configuration covers both the Nile1 and Nile2 areas. The

195 temporal offset in a "tandem" configuration, corresponding to a one-day delay between master and slave

196 images, increases the probability of having high coherence between the available data. Fig. 7 shows the

197 InSAR processing workflow.

198 Before starting interferometric processing, the orbital parameters contained in the scene's metadata were

199 corrected in order to improve the geometric accuracy of the interferometric model and, therefore, the

200 accuracy of the final DEMs. Since ASI did not release precise state vectors of the sensor positions and

201 because metadata contain the most accurate information at the time of delivery, geometric accuracy was

202 improved by using GCPs and modifying the ephemerides of the acquisition time. The coordinates of GCPs

203 were determined during fieldwork and in part derived from Google Earth[TM] images. Although the overall

204 horizontal accuracy of Google Earth's high resolution imagery varies throughout the world, it is generally

205 greater than 10 m for images acquired prior to year 2008 and better for recent acquisitions (Nagi Zomrawi

206 et al., 2013; Paredes-Hernandez et al., 2013; Ubukawa, 2013; Potere, 2008). Recent high resolution images

207 of the Siwa area refer to the years 2011, 2012 and 2014. A large number of spatially well distributed GCPs

208 were then selected in recent images, and possible outliers were removed. According to the literature

209 (Rodriguez et al., 2006) and to checks made using field-mapped GCPs, height values of GCPs (Z coordinate)

210 were automatically derived from the SRTM DEM.

211 After correction of the ephemerides, the master and slave images were coregistered. The pairs of granules

212 were coregistered trying to align the SAR scenes precisely so as to accurately determine phase differences,

213 thereby reducing noise. The procedure consists of two steps: the first "coarse coregistration" refers to

214 "pixel-level" accuracy and uses magnitude information to find the offset and shift of the slave image with

215 respect to the master. The second "sub-pixel coregistration" requires the phase information of SLC images.

216   It is an automatic procedure involving the sub-pixel search for tie points and, after determining the correct

217   transformation equations, slave image resampling. Variable correlation thresholds and grid templates were

218   used and images were subset in order to decrease the computation load by reducing the area to the one

219   investigated. SAR speckle noise was reduced using a Gamma-MAP (or Maximum A Posteriori) filter (Kuan et

220   al., 1987; Lopes et al., 1993). After image coregistration, coherence maps were derived from every

221   interferometric pair. To avoid decorrelation errors that could compromise the calculation of the

222   topographic phase, high coherence values are required to produce interferograms (Ferretti et al., 2007).

223   Decorrelation (especially temporal one) is the main limiting factor for interferometric applications, and it is

224   therefore preferable to use pairs with short temporal baselines (1-2 days maximum) (Zebker and Villasenor,

225   1992). Interferograms were generated for every SAR image pair with the highest coherence values, so that

226   a total of four interferograms (both ascending and descending orbits) were created for Nile1 and Nile2.

227   Range variations can be determined by calculating the phase difference between two SAR images. This

228   difference contains the interferometric phase contribution due to terrain morphology, allowing the

229   construction of a DEM. However, the effect of other factors contributing to this difference must be

230   eliminated. For example, phase flattening removes the flat earth contribution, which depends only on the

231   relative position of the two sensors during acquisition. Flattening facilitates interpretation of the

232   topography in the interferogram phase and reduces phase wrapping complexity. Because the residual

233   phase after flattening is directly proportional to terrain height, the residual interferogram looks much like a

234   contour map of terrain height. Furthermore, some filtering operations helped to remove additional phase

235   noises affecting the interferograms. At this point interferograms contain the topography information

236   measured in cycles of $\pm 2\pi$. In this form, the phase is defined as "wrapped". To calculate the correct

237   elevation of each point, the correct integer number of phase cycles must be added to each phase

238   measurement. The "phase unwrapping" method aims to solve the ambiguities of $\pm 2\pi$ intervals. The applied

239   Minimum Cost Flow (MCF) algorithm (Costantini, 1998) for phase unwrapping is particularly effective for

240   errors on the interferogram due to noise and to low coherence especially. The methodology adopted in this

241   study calls for an a-priori DEM (even one with low spatial resolution) that helps to unwrap the phase in

242   areas for which it is extremely difficult or impossible to complete calculations (i.e. oases). The SRTM DEM

was selected and projected to the SAR reference system; it was then wrapped in a ±2π interval, thereby forming a simulated interferogram. After the unwrapping process, the calculated height data, still in the SAR reference system (range-azimuth and phase variation coordinates), were geocoded to the cartographic map projection (UTM, WGS84 horizontal and vertical Datum, zone 35 north) using image geometry and orbital parameters. Lastly, residual geometric distortions due to the side-looking geometry of radar images were corrected through filtering and bilinear interpolation resampling. The final grid spacing and Z-factor of DEMs are respectively 10 and 1 m (Fig. 8).

3.2 - RADARGRAMMETRY PROCESSING

Radargrammetry involves the elaboration of SAR image pairs acquired from different incidence angles. It was adopted because it is based on stereoscopy using the intensity component instead of phase (Capalbo et al., 2011). For this reason it has, in principle, the advantage over InSAR of being less affected by atmospheric disturbances (Crosetto and Pérez Aragues, 2000; Méric et al., 2009). This technique can be implemented using various look geometry configurations. The "same-side" configuration, with stereo pairs characterized by the same acquisition mode, was adopted in this study. The pairs were acquired with high intersection angles of approximately 10-20°, and a large area of overlap. High intersection angles correspond to high base/height ratios (B/H), which allow better discrimination of elevation differences among adjacent targets. However, since the backscattering of targets varies according to the beam's angle of incidence, scenes acquired with very different incidence angles are unsuitable for radargrammetry because the backscatter response and geometric distortions (e.g. foreshortening) are totally unrelated. Radargrammetry processing therefore entails a compromise between stereo-viewing and elevation discrimination (Toutin and Gray, 2000).

The processing level, product format and polarization of images were the same as those of InSAR images. Fig. 9 shows the radargrammetry workflow.

269   There are analogies with the processing of InSAR images; the accuracy of geometric information was

270   improved by modifying the orbital parameters through GCPs. Granules were subset in order to process only

271   the overlapping areas. SAR scenes were also filtered to reduce the speckle noise that would otherwise

272   decrease the effectiveness of image-matching algorithms used to produce geocoded DEMs (Méric et al.,

273   2009). A Gamma-MAP filter was also applied to the images of the Nile1 and Nile2 areas. Coregistration was

274   required to determine the relative orientation of the image pairs with respect to the reference ones. To

275   accomplish this, GCPs from optical satellite images and tie-points were input both manually and

276   automatically. The exact shifts between match and reference images were determined and used to define

277   (through affine transformations based on coefficients calculated from a least-squares optimization) a quasi-

278   epipolar geometry between the images. This geometric configuration is such that only the terrain x-parallax

279   in the flight direction remains. Tie-points also helped to detect the range of parallax in the area between

280   two stereo pairs, which facilitated the size determination of the search window used for automatic

281   matching. This processing was required to produce a precise disparity map containing the parallax values

282   for each resolution cell of the overlap area. A hierarchical strategy based on pyramidal images resampled

283   from the original ones was adopted to reduce mismatch errors and improve processing accuracy (Méric et

284   al., 2009). The x-parallax values of all points in the disparity maps were processed in order to derive the

285   relative elevation values and produce elevation maps in SAR coordinates. As in the case of the InSAR, data

286   relating to image geometry and orbital parameters was used to geocode these maps and create the

287   radargrammetric DEMs. In all, four DEMs with a 10 m spatial resolution were produced for the Nile1 and

288   Nile2 areas, both in ascending and descending orbit configurations (Fig. 10).

289

290

291   **3.3 - ACCURACY ASSESSMENT**

292

293   All the DEMs produced by SAR interferometry and radargrammetry were assessed for accuracy. This

294   allowed the identification of products with better accuracy to be used in the next steps of spatial analysis.

295   This evaluation was used to highlight the pros and cons of the two adopted techniques. The elevation

296   accuracy of DEMs was assessed using the SRTM model as reference due to its largely documented accuracy

297   and because it was produced through interferometric processing of radar images such as the ones under

298   study. Furthermore, the SRTM model was chosen as reference because good results were achieved from

299   the comparison of its elevation data with GCPs from the GPS survey. Several types of analyses were used to

300   define the accuracy of each DEM: statistical, visual, and spatial. Note that possible errors in DEMs

301   generated from SAR data may be ascribed to:

302   - orbital errors when the exact location of the sensors at the time of acquisition is unknown, leading to

303   inaccuracies in baseline estimation in the case of interferometry and to uncertainties in geometric

304   reconstructions in the case of radargrammetry;

305   - errors due to a large baseline, unsuitable for interferometric pairs, which affects the coherence between

306   images;

307   - errors caused by atmospheric disturbance, which affects the quality of interferometric DEMs especially;

308   - errors due to speckle noise, which affects the accuracy of image matching in radargrammetry;

309   - errors due to different incidence angles, resulting in different backscattering values from the same area in

310   different acquisitions;

311   - errors in coregistration and image processing.

312   Errors can be divided into three categories:

313   - systematic errors, due to procedures and systems used in the generation of the DEMs;

314   - random errors, due to unknown and accidental causes or inaccuracies during processing;

315   - gross errors (blunders), of larger scale and magnitude, easily identified through visual inspection.

316   Landscape features are represented with a high level of detail in DEMs produced by SAR interferometry.

317   These DEMs clearly highlight incisions due to local drainage and structures sculpted by modelling agents.

318   Despite this high level of detail, some areas lack data (void pixels) or contain errors.

319   Although DEMs produced by radargrammetry are much less dense than those produced by interferometry,

320   they are not affected by the systematic errors generally located in wide morphological depressions and

321   oasis water bodies. Overall, radargrammetric DEMs can be used to discern certain morphological details

322   that are invisible on medium-low resolution SRTM and ASTER DEMs.

The accuracy of models, as already said, was determined and statistically analyzed with respect to the SRTM reference DEM. The value of residuals, expressed as the difference in elevation between the SRTM DEM and the one being assessed, was derived through GIS Map Algebra analysis. The accuracy of DEMS is expressed by the mean value, the standard deviation and the Root Mean Square Error (RMSE). Tab.1 shows the statistical parameters calculated for all the DEMs. It proves that, especially for Nile2, all the models have low RMSE values and standard deviations that are less than or nearly equal to the accuracy of the SRTM DEM. Only the DEM of Nile1, provided by SAR interferometry of ascending granules, shows very large statistical errors with respect to the reference DEM. The different attempts to process the image pairs were unsuccessful, and it was impossible to compensate decorrelation (note that we only have an image pair to be processed, so any important decorrelation cannot be solved). Errors in the DEM were easily spotted by visual inspection.

In general, the interferometric products of the Nile1 group yielded the worst results, whereas the radargrammetric DEMs of this group yielded better statistical results. DEMs (both interferometric and radargrammetric) of the Nile2 area have high statistical accuracy. DEMs from radargrammetry data seem to be the most accurate in this area. These results suggest that the combined use of the two techniques may yield better results. Map Algebra operations in a GIS environment allowed the spatialization of the calculated accuracy such that residuals and their magnitude were easily determined and located (Fig. 11).

Tab.2 shows the classification of elevation residuals and their relative percentages.

The spatial analysis of the main differences, characterized by residuals of higher magnitude, reveals how "errors" are mainly located in well defined areas; in the interferometric DEMs, these areas coincide with water bodies, where spatial decorrelation significantly affects elevation model construction. In particular, high residuals are found in the two Siwa and Al-Jaghbub oases and in the small surrounding lakes and vegetated areas.

InSAR in the Nile1 area yielded the worst results; this may be linked to the low coherence between granules and possible mistakes in the reconstruction of the spatial baseline due to inaccuracies in orbital parameters. It may also be affected by temporal decorrelation due to atmospheric interference although the tandem CSKM images of the area refer to May 24 and 25, 2011, when visibility was about 10 km, there

were no precipitation, and the average humidity was around 20% (Weather Underground Inc., 2014).
Nevertheless, atmospheric interference can influence the phase value of the backscatter signal to the sensor, compromising the quality of the DEM derived from interferometry data (Crosetto and Pérez Aragues, 2000).

The good accuracy of DEMs of both areas (Nile1 and Nile2) produced by radargrammetry can be explained, as mentioned earlier, by the lower influence of atmospheric conditions on this technique. However, some residuals are high in areas where the automatic image-matching algorithms failed and, consequently, the morphology was misrepresented. For example, the area covered by the dunes of the Calansho Desert, where both the homogeneity of radiometric backscatter and the risk that the same target changes its radiometric value in different scenes because of the wind, make matching difficult and cause errors in the automatic process.

The intrinsic accuracy of the produced DEMs was assessed by comparing them to each other without considering the reference SRTM DEM. Elevation models derived from data with different acquisition geometries (ascending and descending orbits) and using different techniques (InSAR and radargrammetry) were intersected and the resulting differences in elevation analyzed. This study was done to assess the weight of intrinsic errors caused either by the characteristics of the original image datasets (i.e. baselines, temporal and spatial correlation, acquisition geometry) or by user processing. The residuals of these comparisons are reported in Tab.3, which shows their mean value, standard deviation and RMSE for the Nile2 area. The resulting values are very stable, suggesting that the created models are not affected by errors in processing. Since the DEMs were produced using different input data and processing methods, systematic errors in procedures would affect the different models in different ways and to a different extent. In Tab.3 note that the altitude values in ascending orbit DEMs are always higher (and more accurate, see Tab.1) than those in descending orbit DEMs. This fact may be linked not only to the different geometric characteristics of the baseline, but also to the relationship between the acquisition mode (right-looking in both ascending and descending orbits) and the morphology of the area. DEMs produced from ascending scenes probably provide a more accurate representation of the northwest-southeast trending *garats*, which are orthogonal to the sensor view direction (about 83° N).

377   Considering the vertical accuracy of the reference DEM (±16m LE90), the models produced in this work,

378   thanks to the advanced technology of the COSMO-SkyMed constellation, could be considered very

379   accurate, and the calculated elevation differences could be ascribed to erroneous values of the SRTM DEM;

380   further studies and differential GPS measurements are required to clarify this aspect.

381

382

383   **3.4 - DATA FUSION**

384

385   In order to create a final single DEM of the area with maximum accuracy and reliability, the models from

386   the two areas derived from different techniques were merged using an *ad hoc* GIS procedure. The areas

387   affected by high errors or artefacts were discarded, as well as the pixels or groups of pixels with no

388   elevation values (voids). Data fusion was based on the RMSE derived during accuracy assessment. The eight

389   DEMs were combined and the most accurate values were selected after comparison with the SRTM DEM.

390   Selected values with the lowest residuals were chosen to represent the final elevation of the area, whereas

391   differences greater than or smaller than 10 m were set to "null". The pixels with the greatest vertical

392   accuracy were then mosaiced, and the remaining "null" values were replaced by elevation data from the

393   SRTM DEM appropriately resampled to a 10 m spatial resolution. Lastly, void-filling operations (Reuter et

394   al., 2007) were applied to the mosaic in order to refine the shape of the surface and enhance smoothness

395   and continuity (Fig. 12).

396

397

398   **3.5 - DRAINAGE EXTRACTION**

399

400   The final DEM was used in the morphometric analysis of the area, which aimed to outline the present

401   drainage pattern and possible buried palaeo-channels. The system's resolution and the radar beam's

402   capacity to penetrate thin sand covers are such that it is technically possible to delineate buried

403   hydrographic systems and investigate the palaeo-morphology of arid desert environments (Ghoneim and

404   El-Baz, 2007; Farr et al., 2007).

405   The hydrographic pattern was extracted through an automated procedure based on GIS spatial analysis.

406   The adopted D8 flow direction algorithm (Jenson and Domingue, 1988) is well-suited for the identification

407   of individual channels, channel networks and basin boundaries. The algorithm assigns to each cell of the

408   DEM a value representing the direction to the adjacent cell with the steepest downward slope. The flow of

409   water is traced downhill from all points of the DEM, and the cell value is incremented in a new grid for all

410   the downstream points. Lastly, the drainage network is defined by the relative counts of the cells that have

411   a value greater than a certain threshold. In this paper, following the suggestions of Maidment (2002) for

412   the correct determination of a flow, a threshold of 1% of the maximum cumulative flow was chosen. This

413   threshold increases the area required to generate a channel and therefore less areas will respond the

414   requirements. In this way the number of visible channels decreases, primarily for the benefit of the larger

415   channels and dominant in a basin. Fig. 13 shows the drainage network automatically extracted from the

416   final DEM using this procedure.

417   The resulting drainage lines were assessed by photointerpretation and compared with drainage lines

418   automatically extracted from the SRTM and ASTER DEMs in order to define the final patterns and establish

419   their origin and age as accurately as possible.

420

421

422   **4 - DISCUSSION**

423

424   The final DEM produced from COSMO-SkyMed STRIPMAP images revealed various drainage networks and

425   systems with diverse shapes and characteristics. Results confirm the presence of palaeo-channels in an area

426   extending for more than 4,000 km^2 from the Siwa Oasis, in the east, to the Al-Jaghbub Oasis in the west.

427   The northern area comprises part of the El Diffa Plateau, the southern area negative landforms of the two

428   oases separated by *garats* and sand dunes of the Calansho Desert. Visual inspection of the DEM and

429   satellite imagery clearly reveals an earlier northwest-southeast trending drainage system, nowadays

testified by the presence of aligned *garats* (Fig. 14). In our interpretation, this hydrographic system is related to a big palaeo-drainage involving a large part of the Western Desert. This system is similar to the one west of the study area (in and west of the Qarat Weddah area) described in Carmignani et al. (2009). This drainage cut the Middle and Early Miocene *Marmarica* and *Moghra* carbonate platform formations. Based on the characteristics of the *Sahabi* Formation (Carmignani et al., 1990) in the Gulf of Sirte, Carmignani et al. (2009) referred this earlier system to the Tortonian-Early Messinian (Fig. 4). Fig. 15 shows the hypothesized pattern of the drainage network during the Late Messinian salinity crisis from Asyut (Egypt) up to the Gulf of Sirte.

The automatic drainage lines extracted from the CSKM DEM (Fig. 13) do not include the earlier northwest-southeast bedrock incision pattern because of the chosen flow accumulation threshold and the actual topography. On the contrary, they delineated a different system consisting of two networks with different shapes, catchment areas and flow directions. The first, located in the Nile2 area, comprises the Al-Jaghbub Oasis and flows to the W-NW, joining the westernmost systems of Carmignani et al. (2009); the second, in the surroundings of Siwa (Nile1 area) flows to the E-SE, joining the easternmost systems photointerpreted by the same authors south of the Qattara Depression (Fig. 4). The morphology of these networks is markedly different from the erosional system pre Mediterranean Sea drawdown. The watershed separating the two drainage lines extracted from the CSKM DEM is clearly identified west of Siwa Oasis (Fig. 13). This feature, which was practically imperceptible in the field and in earlier remotely sensed data, represents the geographical divide between the two drainage systems in the area. The automatically extracted drainage lines are probably related to the peculiar setting of north Africa in the Late Messinian. During this period, the important marine regression that affected the Mediterranean Sea changed the entire physiography of the area and, consequently, its regional hydrography (Ryan and Cita, 1978). Due to the change in topographic gradient, headward erosion cut new channels in the bedrock that were later partially buried by Pliocene and Quaternary deposits (Said, 1962). At this stage, two drainage networks developed in opposite directions (Fig. 16). One system flowed westward and is still visible in Libya from the area north of Qarat Weddah up to the old Sahabi lagoon (Fig. 15); the palaeo-channels clearly cut the drainage pre Mediterranean Sea salinity crisis. *Wadi al Hamim* and *Wadi al Maqar*, described in Carmignani (1984),

17

457 Giglia (1984), and Giammarino (1984), are two examples of channels carved in the Middle Miocene

458 Cyrenaica carbonate platform. In the Sirte area these palaeo-channels flowed into the Sahabi channel (Barr

459 and Walker, 1973), a canyon with a depth of about 400 m and a width of 5 km carved in the carbonate

460 platform. Griffin (2011) uses the name Eosahabi for this channel of Messinian age and older, while the term

461 Sahabi is used by the author for a river system of Pliocene age and younger.

462 At the same time headward erosion reached the Al-Jaghbub Oasis, where, thanks to the network

463 automatically extracted from CSKM data, the uppermost section of the Libyan Late Messinian drainage can

464 be identified. Drainage around the Al Jaghbub Oasis, which roughly corresponds to the Nile2 area, is

465 therefore probably associated with this system.

466 A second system flowed eastward, forming deep canyons that are in part still visible along the course of the

467 present Nile River (i.e. Asyut, Aswan in Egypt – Fig. 1). In our hypothesis, this system captured first the

468 Miocene palaeo-Nile south of the Qattara Depression and then its upstream portion near Asyut, totally

469 cutting off the previous drainage and forming the present course of the Nile River. In this system, surface

470 waters of the North Western Desert were conveyed to the sea in deep canyons (at the time the base-level

471 was significantly lower than the present one); north of Cairo, these incisions reached a depth greater than

472 2,500 m (Choumakov, 1967; Said, 1990) and are now filled by Plio-Quaternary sediments. The drainage

473 automatically extracted from the CSKM DEM of the Nile1 area, in the surroundings of Siwa, must be related

474 to this Late Messinian system. Because the pattern and direction of this drainage is similar to that

475 photointerpreted in the Qattara Depression, it may represent either the Late Messinian palaeo-Nile or one

476 of its left-bank tributaries. We therefore suggest that they belonged to the same drainage system, although

477 additional information is required, particularly for the area between Nile1 and Qattara Depression.

478 During the Pliocene a marine transgression occurred throughout the Mediterranean area (Ryan and Cita,

479 1978); the deposits (e.g. *Qarat Weddah* Formation in Libya) completely covered the Miocene carbonate

480 platform and its drainage systems (both the Late Messinian canyons and the remains of the previous

481 system – Fig. 17). At that age, the channel Sahabi was not as deep as the Nile canyons because probably

482 already deactivated by a river capture that occurred to the south (this would also explain the different

483 thickness of the Pliocene deposits that are found at the same latitudes in the two palaeo-valleys).

South of Qarat Weddah, a river system characterized by a large fan that covered the southernmost portions of the pre-Messinian drainage (the Sarir Dalmah alluvial fan of Pachur and Altmann, 2006) transported the sands produced by the erosion of the Nubian sandstones (cropping out extensively in southern Libya). These sands formed the Pliocene sediments that lie disconformably above the Miocene carbonate platform and buried its surface drainage channels.

At the same time, in Egypt, the Pliocene transgression affected the Late Messinian canyons of the Nile River; the rise in sea level formed a narrow gulf reaching up to Aswan (Said, 1990), flooding completely the current delta. The deposits of this period are well documented and contain rich marine faunas (Said, 1990). Later, during the Quaternary, a new regression reactivated the Late Messinian drainage system (Fig. 18). The Quaternary regression, dated to the Tyrrhenian (Late Pleistocene) was less incisive than the Late Messinian one, and the original canyons maintained the thick Pliocene deposits that the new rivers failed to completely erode (Carmignani et al., 1990). Nevertheless, the climate became very arid and, starting in the Early Pleistocene, wide areas of northeast Africa became desertic. The trade winds partially eroded the Pliocene sediments lying above the palaeo-drainage (Brookes, 2001) and deposited them to the south, forming the sand sheet deposits and dunes of the Calansho Desert, even reaching the Tibesti Plateau about 1,000 km south of the Gulf of Sirte. Wind bared the northern areas especially, revealing structures pertaining to the earlier drainage systems, modelling the present-day *garats,* and uncovering traces of ancient, fossil river beds. According to Di Cesare et al. (1963), during the Quaternary pluvial stages (i.e. Saharan I and II of Mousterian - Said, 1990), drainage was from south to north and was partially superimposed on the Late Messinian network.

The proposed chronological evolution of the Siwa area is also supported by the presence of well-preserved morphological features such as the *garats*, typical of this area. These were formed by the erosive action of a big river acting before the Late Messinian. During the Late Messinian this area was not deeply eroded due to its proximity to the watershed that preserved the older morphological landscape. There was probably no intense erosion of the Siwa area in the following epochs.

511   **CONCLUSIONS**

512

513   SAR interferometry and radargrammetry applied to high spatial resolution images from the COSMO-

514   SkyMed constellation were successfully used to create the digital elevation model and trace the drainage

515   network in the Siwa area. The catchment areas of two networks were delimited and the watershed

516   between the "Libyan" system, flowing westward to the Sirte area, and the "Egyptian" one, flowing

517   eastward, was identified.

518   Recent attempts to identify and extract the detected hydrography from other DEMs such as SRTM and

519   ASTER were unsuccessful. The photointerpretation of high-resolution passive optical imagery did not reveal

520   such morphological detail. Moreover, thanks to the penetrative capabilities of the radar beam, the

521   southern part of automatically extracted drainage lines shows a prevailing northward direction of flow.

522   These drainage networks (located in the area covered by the Calansho and Western deserts sand sheet -

523   Figs. 13 and 18) could be linked to the Quaternary regression phase during which the ancient drainage was

524   reactivated, as documented by Di Cesare et al. (1963).

525   The reported results provide additional important data and evidence in support of the hypothesis proposed

526   by Carmignani et al. (2009). Results also provide new starting points for future detailed geological and

527   palaeo-environmental studies of the area. The idea that there was a palaeo-Nile flowing from Egypt to the

528   Gulf of Sirte, in Libya, is very striking but needs to be confirmed by additional data. Further research,

529   including fieldwork, geophysical investigation and processing of additional high-resolution radar data, in the

530   area between the Nile1 and Qattara Depression areas may clarify the physiography of these drainage

531   systems and, in general, the global palaeo-hydrographic setting of north-eastern Africa. This paper confirms

532   how remotely sensed data can be a fundamental tool and source of information for the analysis of vast and

533   remote areas.

534

535

REFERENCES

Abdel-Fattah, Z.A., Kora, M.A., & Ayyad, S.N. (2013). Facies architecture and depositional development of Middle Miocene carbonate strata at Siwa Oasis, Northwestern Egypt. Facies, 59(3), 505-528, http://dx.doi.org/10.1007/s10347-012-0332-2.

ASI (2009). COSMO-SkyMed SAR Products Handbook.

Barr, F.T., & Walker, B.R. (1973). Late Tertiary channel system in northern Libya and its implications on Mediterranean sea level changes. Initial Reports of the Deep Sea Drilling Project, 13, 1244-1250.

Brookes, I.A. (2001). Aeolian erosional lineations in the Libyan desert, Dakhla region, Egypt. Geomorphology, 39(3), 189-209, http://dx.doi.org/10.1016/S0169-555X(01)00026-5.

Capaldo, P., Crespi, M., Fratarcangeli, F., Nascetti, A., & Pieralice, F. (2011). DSM generation from high resolution COSMO-SkyMed imagery with radargrammetric model . In: ISPRS Hannover WorkShop 2011 high-resolution Earth Imaging for Geospatial Information. The International Archives of the Photogrammetry, Remote Sensing and Spatial Information Sciences, Vol. XXXVIII-4/W19, Heipke, C.; Jacobsen, K.; Rottensteiner, F.; Müller, S.; Sörgel, U., ISSN: 1682-1777, Hannover (Germany), June 14-17, 2011.

564   Carmignani, L. (1984). Geological Map of Libya, Explanatory Booklet, Sheet: Wadi al Hamim, NH 34-7.

565   Tripoli (Libya): Industrial Research Centre.

566

567   Carmignani, L., Giammarino, S., Giglia, G., & Pertusati, P. (1990). The Qasr as Sahabi succession and the

568   Neogene evolution of the Sirte Basin (Libya). Journal of African Earth Sciences, 10(4), 753-769,

569   http://dx.doi.org/10.1016/0899-5362(90)90042-D.

570

571   Carmignani, L., Salvini, R., & Bonciani, F. (2009). Did the Nile River flow to the Gulf of Sirte during the late

572   Miocene? Italian Journal of Geosciences, 128(2), 403-408, http://dx.doi.org/10.3301/IJG.2009.128.2.403.

573

574   Choumakov, I. S. (1967). Pliocene and Pleistocene deposits of the Nile Valley in Nubia and Upper Egypt.

575   Academy of Science of the USSR, transaction of the Geological Institute, 170, 1-110.

576

577   Costantini, M. (1998). A novel phase unwrapping method based on network programming. IEEE

578   Transactions on Geoscience and Remote Sensing, 36(3), 813-821, http://dx.doi.org/10.1109/36.673674.

579

580   Crosetto, M., & Pérez Aragues, F. (2000). Radargrammetry and SAR Interferometry for DEM Generation:

581   Validation and Data Fusion. Proceedings of CEOS SAR workshop, ESA SP-450, 367-373.

582

583   Di Cesare, F., Franchino, A., & Sommaruga, C. (1963). The Pliocene-Quaternary of Giarabub Erg Region.

584   Proceedings of First Sharan Symposium. Revue de l'Institut Francais Du Petrole, 18, 10-11.

585

586   Farr, T., Rosen, P., Caro, E., Crippen, R., Duren, R., Hensley, S., Kobrick, M., Paller, M., Rodriguez, E., Roth, L.,

587   Seal, D., Shaffer, S., Shimada, J., Umland, J., Werner, M., Oskin, M., Burbank, D., & Alsdorf, D. (2007). The

588   Shuttle Radar Topography Mission. Reviews of Geophysics, 45(2), 2-43,

589   http://dx.doi.org/10.1029/2005RG000183.

590

591 Ferretti, A., Monti-Guarnieri, A., Prati, C., Rocca, F., & Massonnet, D. (2007). Part A: Interferometric SAR

592 image processing and interpretation. In: Fletcher, K. (eds) InSAR Principles: Guidelines for SAR

593 Interferometry Processing and Interpretation. Noordwijk (The Netherlands): ESA Publications Division

594 (http://www.esa.int/esapub/tm/tm19/TM-19_ptA.pdf).

595

596 Ghoneim, E., & El-Baz, F. (2007). The application of radar topographic data to mapping of a mega-

597 paleodrainage in the Eastern Sahara. Journal of Arid Environments, 69(4), 658-675,

598 http://dx.doi.org/10.1016/j.jaridenv.2006.11.018.

599

600 Giammarino, S. (1984). Geological Map of Libya, Explanatory Booklet, Sheet: Wadi al Khali, NH 34-8. Tripoli

601 (Libya): Industrial Research Centre.

602

603 Giglia, G. (1984). Geological Map of Libya, Explanatory Booklet, Sheet: Ajdabiya, NH 34-6. Tripoli (Libya):

604 Industrial Research Centre.

605

606 Griffin, D.L. (2011). The late Neogene Sahabi rivers of the Sahara and the hamadas of the eastern Libya–

607 Chad border area. Palaeogeography, Palaeoclimatology, Palaeoecology, 309(3–4), 176-185,

608 http://dx.doi.org/10.1016/j.palaeo.2011.05.007.

609

610 Jenson, S.K., & Domingue, J.O. (1988). Extracting topographic structure from digital elevation data for

611 geographic information system analysis. Photogrammetric engineering and remote sensing, 54(11), 1593-

612 1600.

613

614 Klitzsch, E., List, F., & Pohlmann, G. (1987). Geological map of Egypt (1:500,000 - 24 sheets). Cairo (Egypt):

615 Conoco Coral and Egyptian General Petroleum Corporation.

616

617 Kuan, D.T., Sawchuk, A.A., Strand, T.C., & Chavel, P. (1987). Adaptive Restoration of Images with Speckle.

618 IEEE Transactions on Acoustics, Speech, and Signal Processing, 35(3), 373-383,

619 http://dx.doi.org/10.1109/TASSP.1987.1165131.

620

621 Lopes, A., Nezry, E., Touzi, R., & Laur, H. (1993). Structure detection and statistical adaptive speckle filtering

622 in SAR images. International Journal of Remote Sensing, 14(9), 1735-1758,

623 http://dx.doi.org/10.1080/01431169308953999.

624

625 Maidment D.R. (2002). Arc Hydro: GIS for water resources, vol. 220. ESRI press, Redlands, 203 pp.

626

627 McCauley, J.F., Breed, C.S., Schaber, G.G., Mchugh, W.P., Issawi, B., Haynes, C.V., Grolier, M.J., & Kilani, A.E.

628 (1986). Paleodrainages of the Eastern Sahara-The Radar Rivers Revisited. IEEE Transactions on Geoscience

629 and Remote Sensing, GE-24(4), 624-648, http://dx.doi.org/10.1109/TGRS.1986.289678.

630

631 McCauley, J.F., Schaber, G.G., Breed, C.S., Grolier, M.J., Haynes, C.V, Issawi, B., Elachi, E., & Blom, R. (1982).

632 Subsurface valleys and geoarcheology of the eastern Sahara revealed by Shuttle radar. Science, 218(4576),

633 1004-1020, http://dx.doi.org/10.1126/science.218.4576.1004.

634

635 Méric, S., Fayard, F., & Pottier, E. (2009). Radargrammetric SAR image processing. Geoscience and Remote

636 Sensing. In: Pei-Gee Peter Ho (Eds.), Geoscience and Remote Sensing, Intech pp. 421–454,

637 http://dx.doi.org/10.5772/8300.

638

639 Nagi Zomrawi, M., Ahmed, G. & Hussam Eldin, M. (2013). Positional Accuracy Testing of Google Earth.

640 International Journal of Multidisciplinary Sciences and Engineering, 4(6), 6-9.

641

642 Pachur, H.J., Altmann, N. (2006). Die Ostsahara im Spätquartär: Ökosystemwandel im größten hyperariden

643 Raum der Erde. Springer, Berlin.

644

Paillou, P., Schuster, M., Tooth, S., Farr, T., Rosenqvist, A., Lopez, S., & Malezieux, J.M. (2009). Mapping of a major paleodrainage system in eastern Libya using orbital imaging radar: The Kufrah River. Earth and Planetary Science Letters, 277 (3-4), 327-333, http://dx.doi.org/10.1016/j.epsl.2008.10.029.

648

Paredes-Hernandez, C.U., Salinas-Castillo, W.E., Guevara-Cortina, F., & Martinez-Becerra, X. (2013). Horizontal positional accuracy of Google Earth's imagery over rural areas: a study case in Tamaulipas, Mexico. Boletim de Ciências Geodésicas, 19(4), 588-601.

652

Potere, D. (2008). Horizontal positional accuracy of Google Earth's high-resolution imagery Archive. Sensors, 8 (12), 7973-7981, http://dx.doi.org/10.3390/s8127973.

655

Reuter, H.I., Nelson, A., & Jarvis, A. (2007). An evaluation of void-filling interpolation methods for SRTM data. International Journal of Geographical Information Science, 21(9), 983-1008, http://dx.doi.org/10.1080/13658810601169899.

659

Robinson, C.A., El-Baz, F., Al-Saud, T.S.M., & Jeon, S.B. (2006). Use of radar data to delineate palaeodrainage leading to the Kufra Oasis in the Eastern Sahara. Journal of African Earth Sciences, 44(2), 229-240, http://dx.doi.org/10.1016/j.jafrearsci.2005.10.012.

663

Rodriguez, E., Morris, C.S., & Belz, J.E. (2006). A Global Assessment of the SRTM Performance. Photogrammetric Engineering and Remote Sensing, 72(3), 249-260.

666

Ryan, W.B.F., & Cita, M.B. (1978). The nature and distribution of Messinian erosional surfaces. Indicators of a several-kilometer-deep Mediterranean in the Miocene. Marine Geology, 27(3-4), 193-230, http://dx.doi.org/10.1016/0025-3227(78)90032-4.

670

671   Said, R. (1962). The Geology of Egypt. New York (United States): Elsevier, 377 pp..

672

673   Said, R. (1990). The Geology of Egypt. Taylor & Francis Group.

674

675   Schaber, G.G., McCauley, J.F., & Breed, C.S. (1997). The use of multifrequency and polarimetric SIR-C/X-SAR

676   data in geologic studies of Bir Safsaf, Egypt. Remote Sensing of Environment, 59(2), 337-363,

677   http://dx.doi.org/10.1016/S0034-4257(96)00143-5.

678

679   Szczechura, J., & Abd-Elshafy, E. (1988). Ostracodes and foraminifera from the Middle Miocene of the

680   western coast of the Gulf of Suez, Egypt. Acta Palaeontologica Polonica, 33(4), 273–342.

681

682   Tawadros, E. (2001). Geology of Egypt and Libya. Taylor & Francis Group.

683

684   Toutin, T., & Gray, L. (2000). State-of-the-art of elevation extraction from satellite SAR data. ISPRS Journal

685   of Photogrammetry and Remote Sensing , 55(1), 13-33, http://dx.doi.org/10.1016/S0924-2716(99)00039-8.

686

687   Ubukawa, T. (2013). An evaluation of the horizontal positional accuracy of Google and Bing satellite

688   imagery and three roads data sets based on high resolution satellite imagery. New York: Center for

689   International Earth Science Information Network (CIESIN), Earth Institute Columbia University, 16 pp..

690

691   Weather Underground Inc. (2014). Available online at http://www.wunderground.com (last accessed July

692   2014)

693

694   Youssef, A.M. (2009). Mapping the mega paleodrainage basin using shuttle radar topography mission in

695   Eastern Sahara and its impact on the new development projects in Southern Egypt. Geospatial Information

696   Science, 12(3), 182-190, http://dx.doi.org/10.1007/s11806-009-0057-8.

697

698 Zebker, H.A., & Villasenor, J. (1992). Decorrelation in interferometric radar echoes. IEEE Transactions on

699 Geoscience and Remote Sensing, 30(5), 950-959, http://dx.doi.org/10.1109/36.175330.
700

701

FIGURE CAPTIONS

703 Fig. 1 – Location map; red box outlines the study area.

704 Fig. 2 – Subset of the Geological Map of Egypt; 1:500,000 scale, Sheet Siwa NH 35 SW (digitized from

705 Klitzsch et al., 1987).

706 Fig. 3 – Examples of *garats* in the surroundings of Siwa (little mesas in A and B, buttes in C and D). Inset

707 map shows the location of these geomorphologic landscapes.

708 Fig. 4 - Sketch map showing the possible course of the palaeo-Nile river during the Miocene (modified from

709 Carmignani et al., 2009); the violet box indicates the location of the study area.

710 Fig. 5 – Location of the available CSKM scenes.

711 Fig. 6 – Examples of footprint and quick look of CSKM descending scenes for areas Nile1 (top) and Nile2

712 (bottom).

713 Fig. 7 - InSAR processing workflow.

714 Fig. 8 –InSAR DEMs; the Nile1 and Nile2 areas in both ascending and descending orbit configurations.

715 Fig. 9 - Radargrammetry workflow.

716 Fig. 10 – Radargrammetry DEMs; the Nile1 and Nile2 areas in both ascending and descending orbit

717 configurations.

718 Fig. 11 – Example of differences in elevation between the SRTM DEM and the DEMs of the Nile2 area,

719 calculated from granules in descending orbit using interferometry (left) and radargrammetry (right).

720 Fig.12 - 1Final DEM of the study area.

721 Fig. 13 – Drainage network extracted from the final DEM.

722 Fig.14 – Area characterized by the northwest-southeast trending drainage system (Quickbird scene from

723 Google Earth™ in background); inset map shows a detailed view of the *garats* area.

724 Fig. 15 – Hypothesized pattern of the drainage network before the Late Messinian drawdown of the

725 Mediterranean Sea.

726 Fig. 16 – Hypothesized pattern of the drainage network during the Late Messinian.

727 Fig. 17 – Hypothesized pattern of the drainage network during the Pliocene.

728 Fig. 18 – Hypothesized pattern of the drainage network during the Quaternary.

729

730

731 **TABLES**

732 Tab.1 – Statistics of elevation differences between the produced DEMs and the SRTM.

NILE 1		Mean (m)	Std. Dev. (m)	RMSE (m)
INSAR	Ascending	37	160	132
RADARGRAMMETRY	Ascending	3	13	12
INSAR	Descending	-19	19	22
RADARGRAMMETRY	Descending	-3	19	17
NILE 2		Mean (m)	Std. Dev. (m)	RMSE (m)
INSAR	Ascending	3.9	10	9
RADARGRAMMETRY	Ascending	1	8	8
INSAR	Descending	-7	12	12
RADARGRAMMETRY	Descending	-6	9	10

733

734 Tab.2 - Classification of elevation residuals and relative percentages.

Range of residuals (m)		Nile1 Ascending Interferom.	Nile1 Ascending Radargramm.	Nile1 Descending Interferom.	Nile1 Descending Radargramm.	Nile2 Ascending Interferom.	Nile2 Ascending Radargramm.	Nile2 Descending Interferom.	Nile2 Descending Radargramm.
	Min - -40	36.3%	0.1%	16.7%	0.8%	0.0%	0.0%	1.7%	0.7%
	-40 - -30	2.5%	0.4%	18.5%	2.1%	0.2%	0.1%	3.4%	1.5%
	-30 - -20	2.5%	1.6%	15.8%	12.2%	1.2%	1.3%	10.8%	4.8%
	-20 - -10	2.2%	11.9%	15.2%	32.2%	6.7%	7.2%	24.1%	21.4%
	-10 - 0	2.1%	29.4%	14.3%	23.6%	28.7%	35.1%	32.4%	58.8%
	0 - 10	2.0%	29.5%	12.7%	12.8%	39.1%	44.1%	20.3%	9.3%
	10 - 20	2.1%	16.2%	5.4%	5.6%	19.4%	10.1%	6.6%	2.0%

28

20 - 30	2.1%	6.5%	1.0%	3.4%	3.3%	1.7%	0.7%	0.9%
30 - 40	2.1%	2.7%	0.3%	2.4%	0.9%	0.3%	0.1%	0.3%
40 - Max	46.1%	1.7%	0.1%	4.9%	0.5%	0.1%	0.1%	0.2%
	100.0%	100.0%	100.0%	100.0%	100.0%	100.0%	100.0%	100.0%

735

736   Tab.3 – Statistics of elevation differences among the produced DEMs of the Nile2 area (ascending orbit -

737   descending orbit).

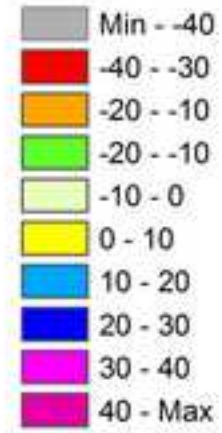| NILE2		Mean (m)	Std. Dev. (m)	RMSE (m)
INSAR ASCENDING	INSAR DESCENDING	-14	12	13
RADARGRAMMETRY ASCENDING	RADARGRAMMETRY DESCENDING	-7	10	10
RADARGRAMMETRY ASCENDING	INSAR DESCENDING	-14	12	15
INSAR ASCENDING	RADARGRAMMETRY DESCENDING	-12	12	12

738

Figure 1
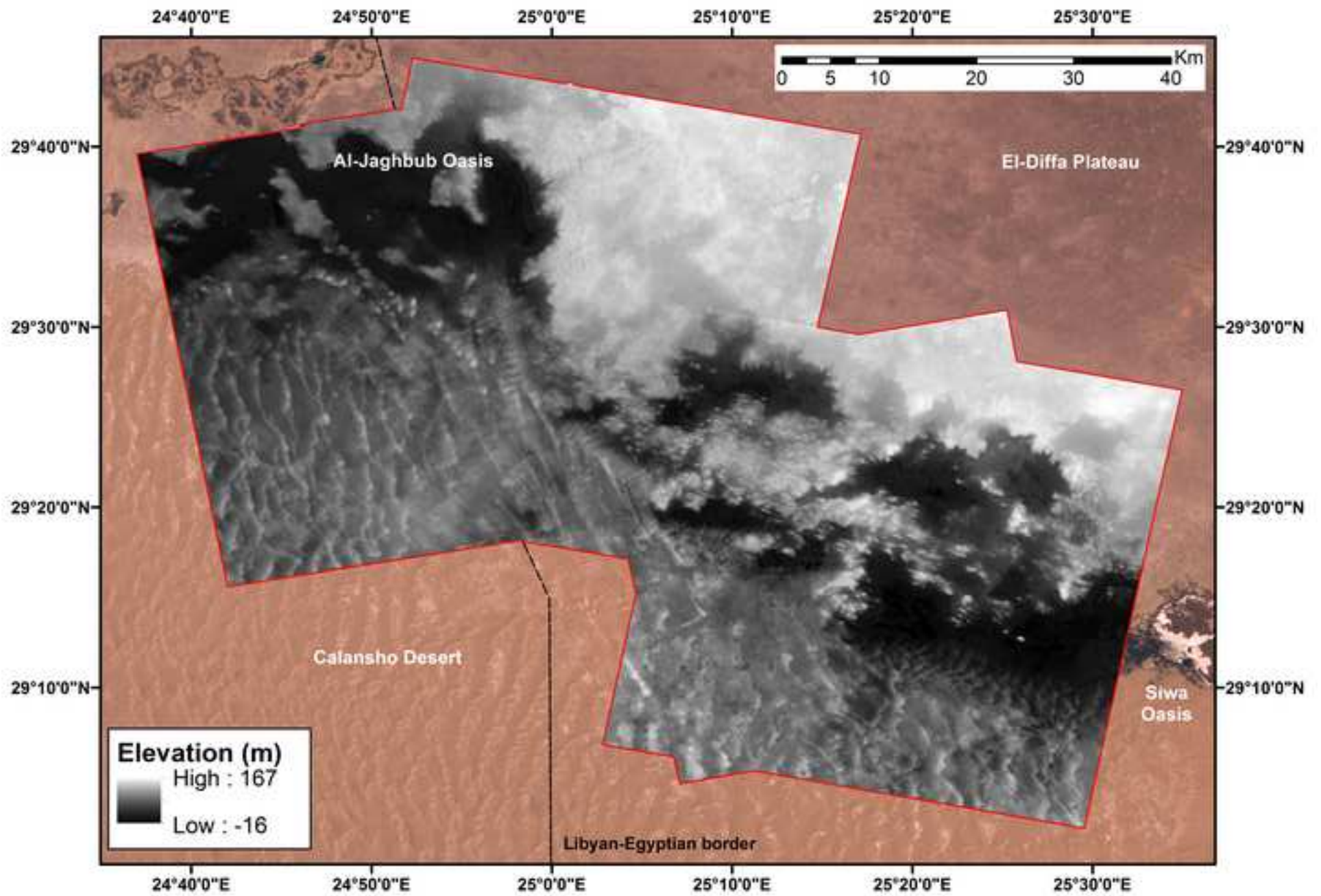**Click here to download high resolution image**
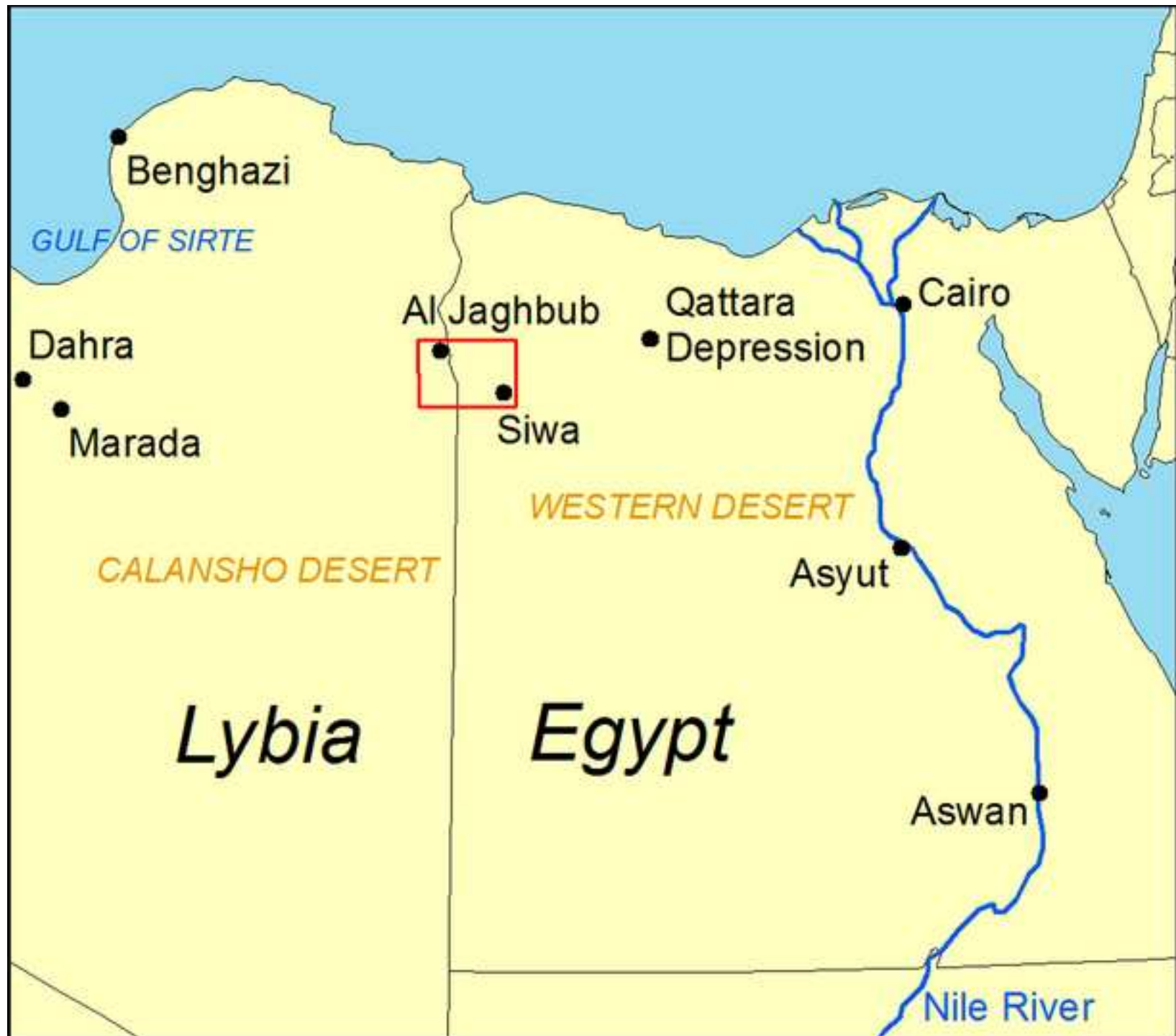
Figure 2
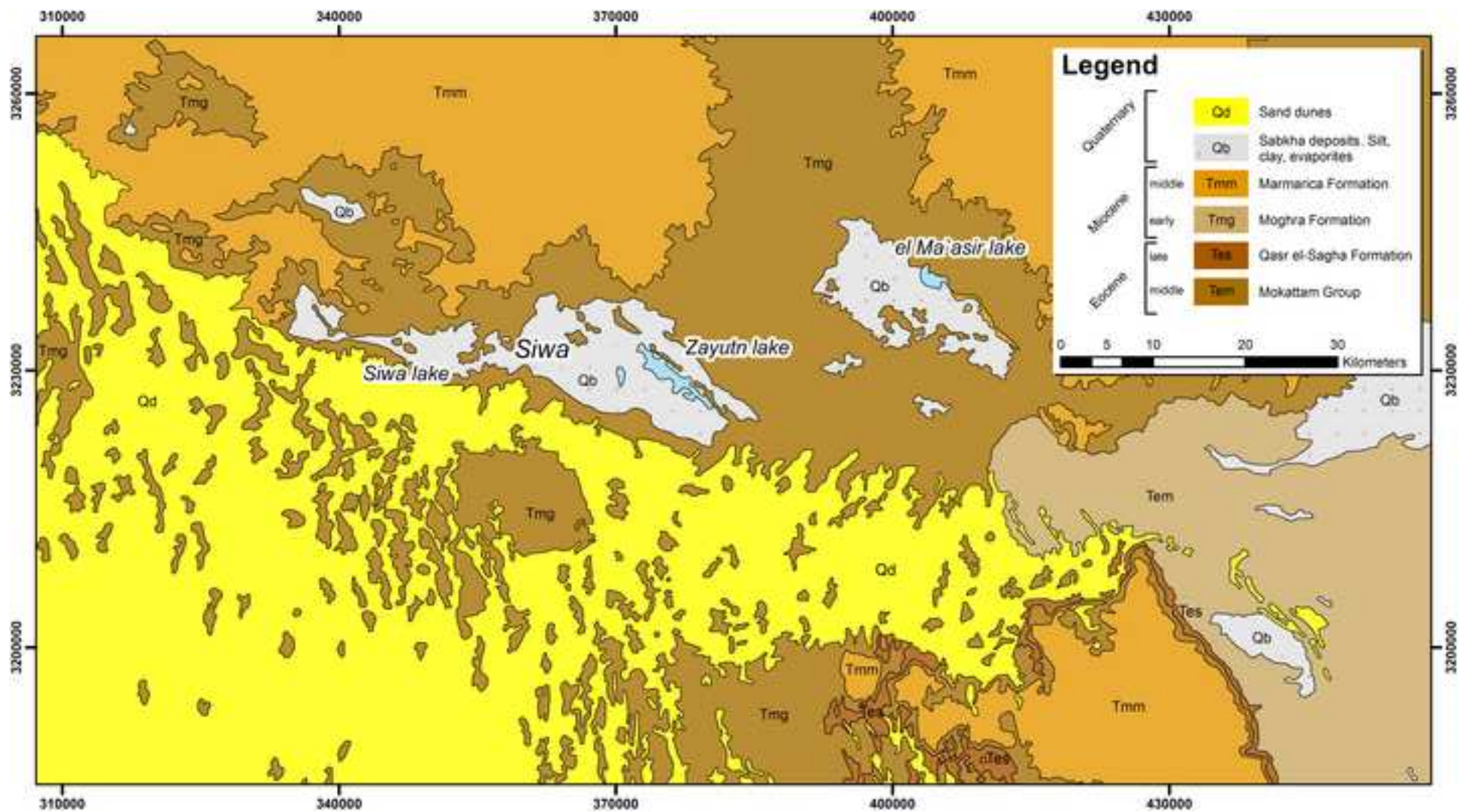
Figure 3
[Click here to download high resolution image](#)
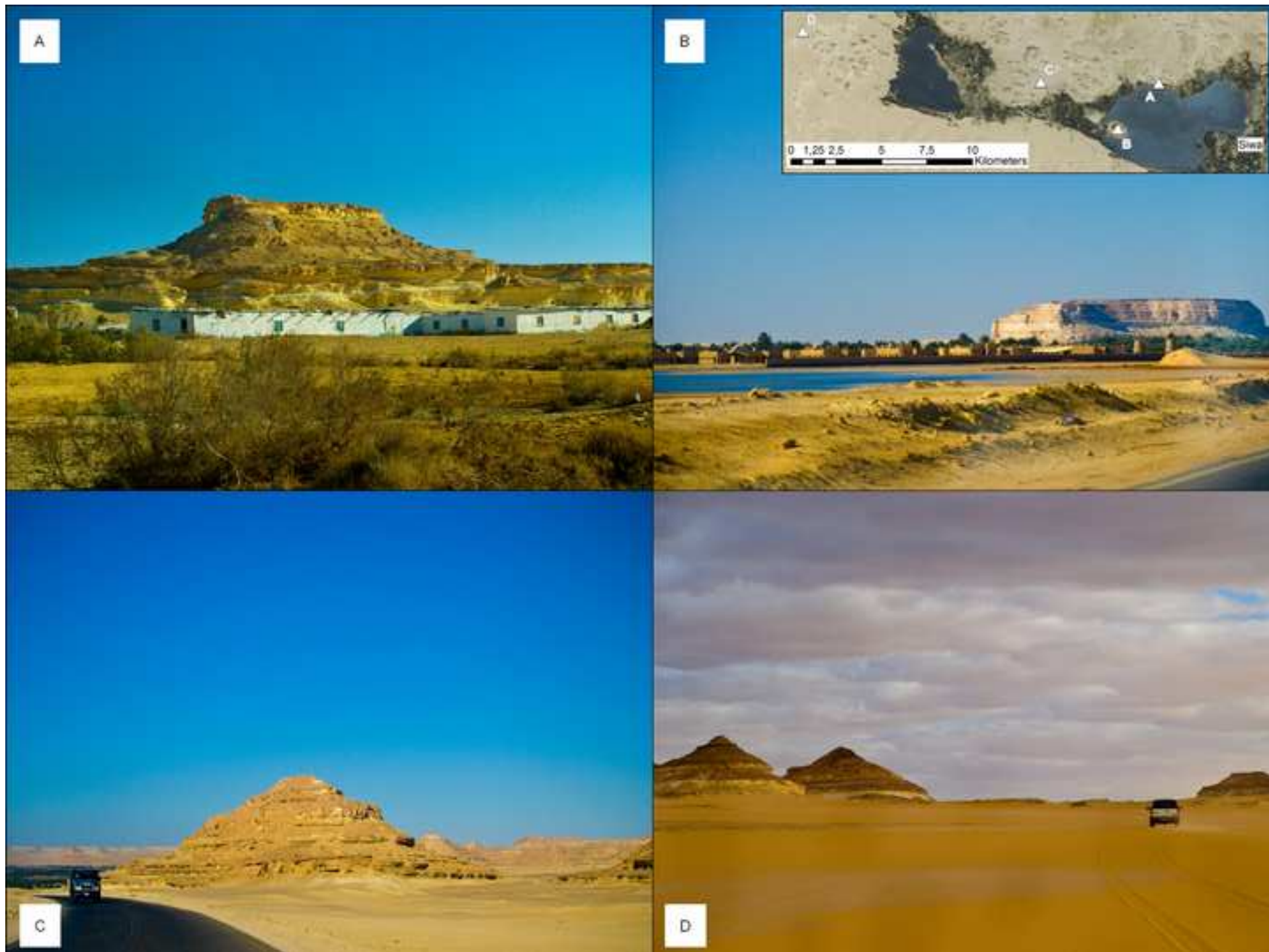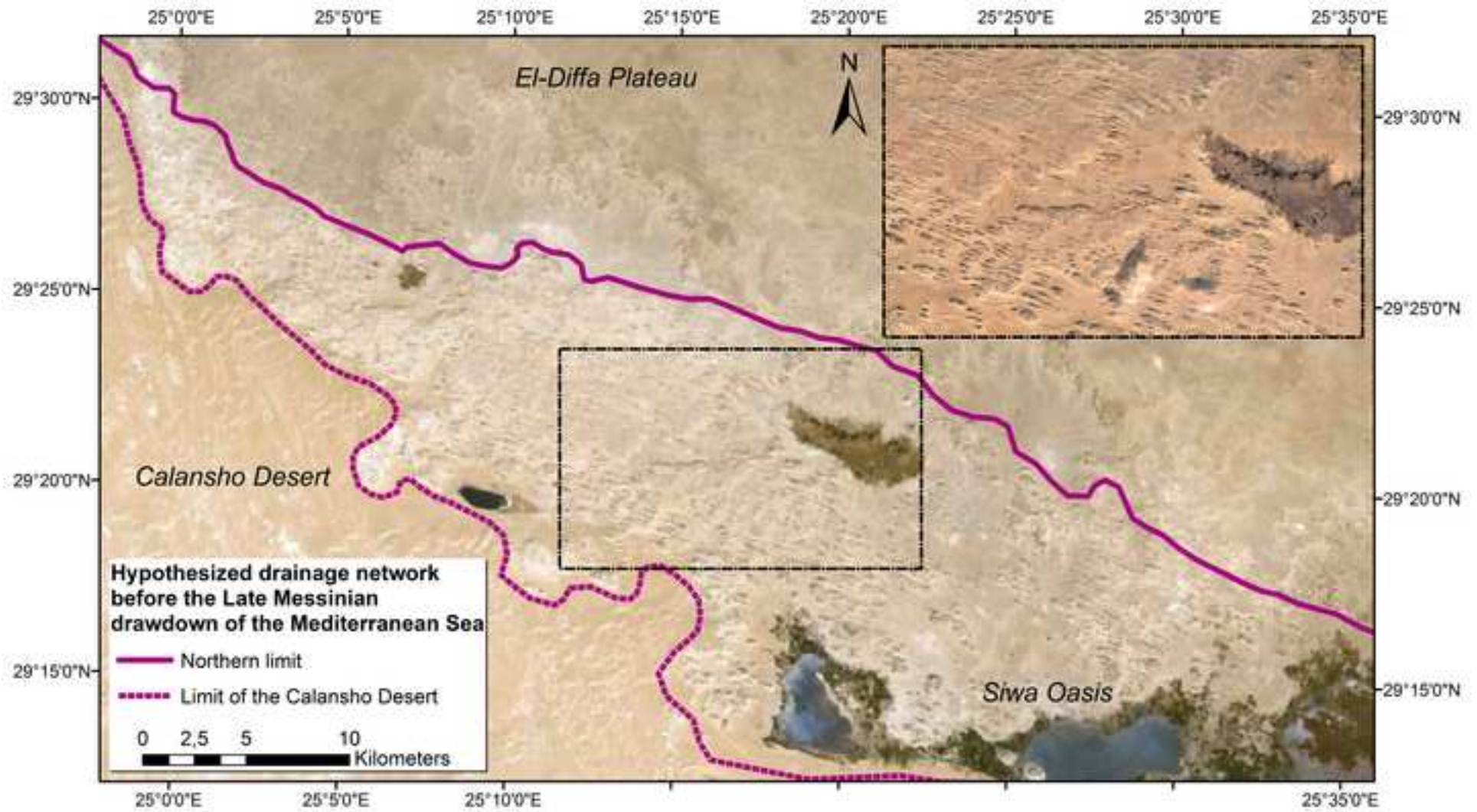
Figure 4
Click here to download high resolution image
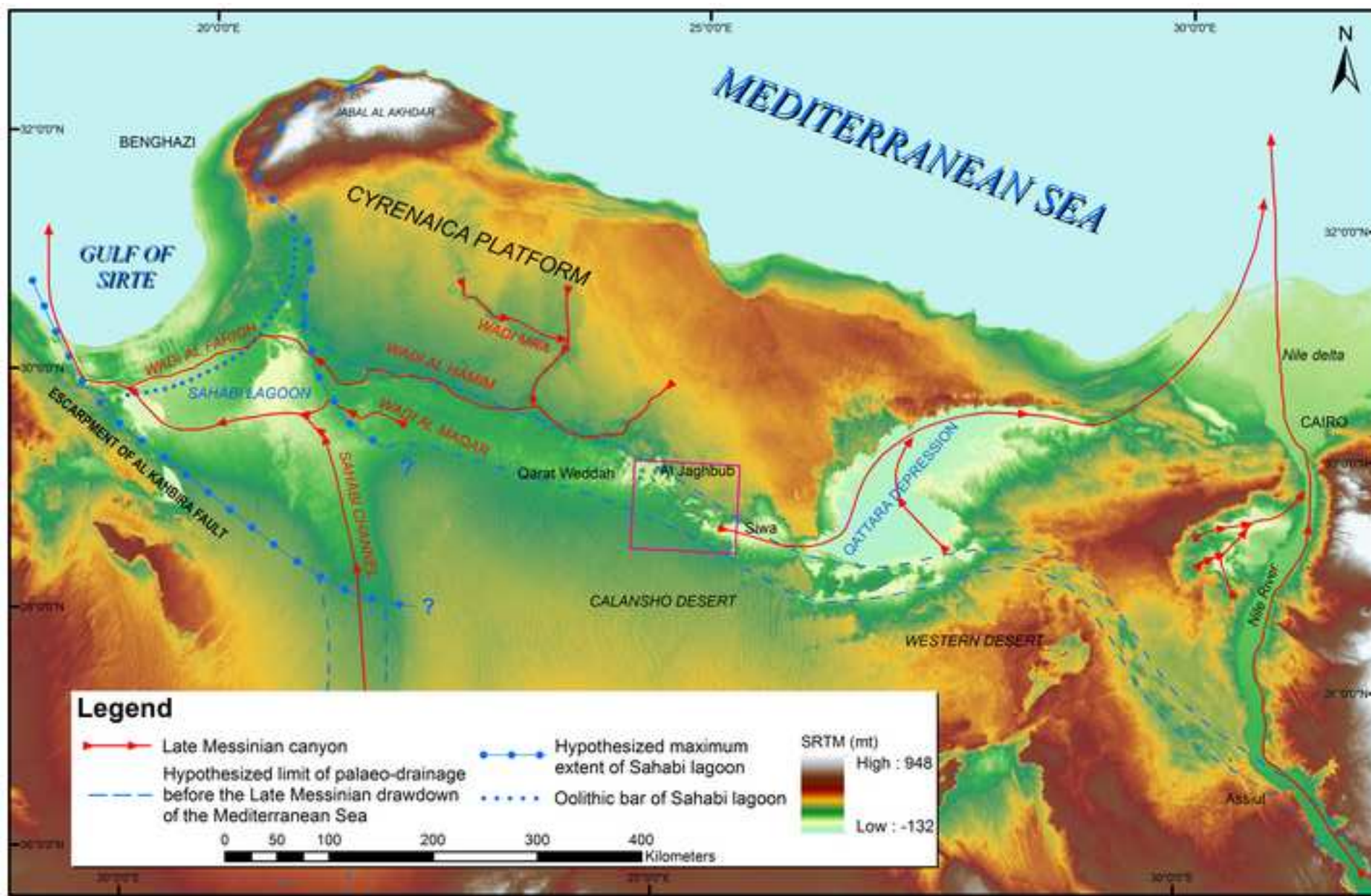
Figure 5
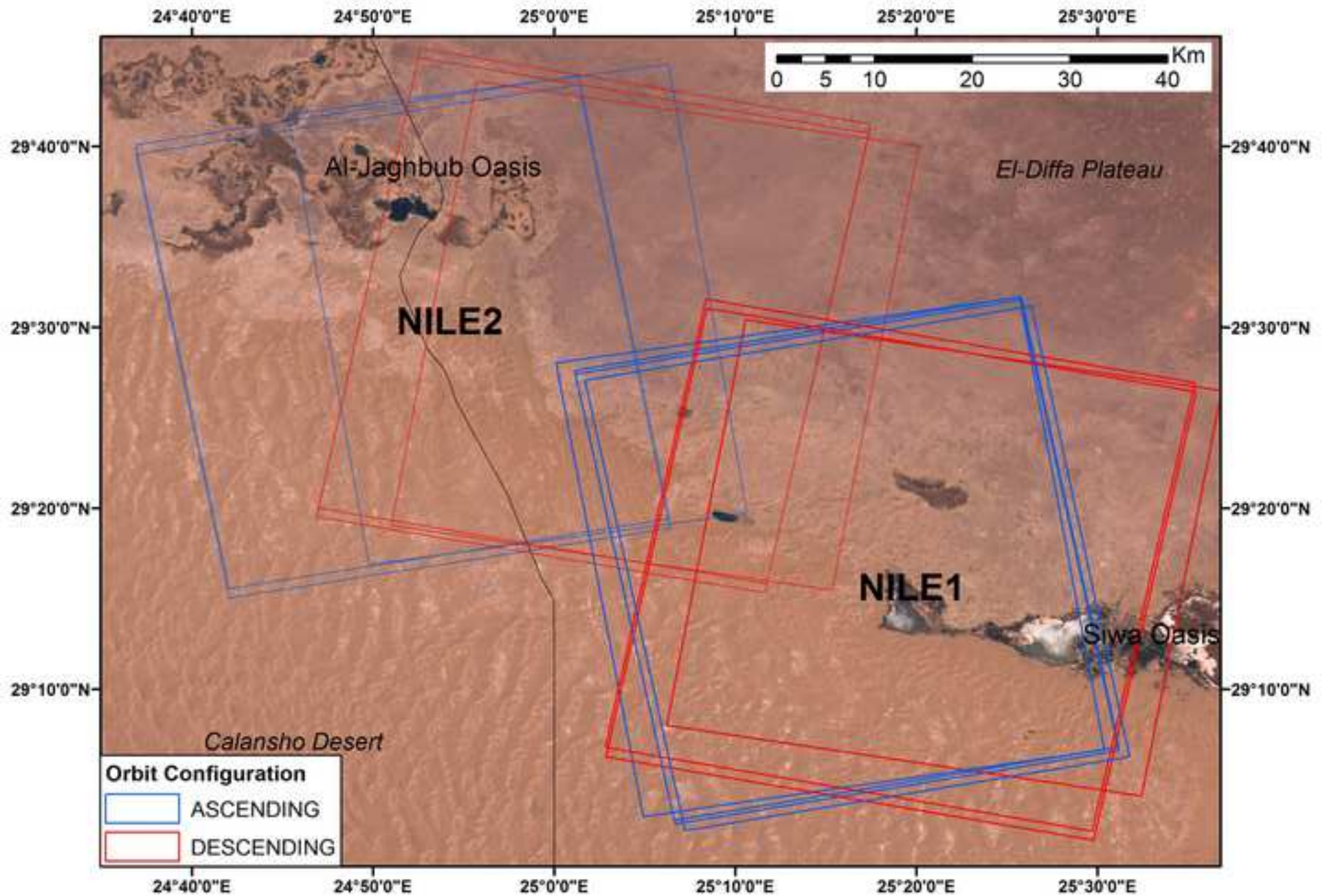
Figure 6
Click here to download high resolution image
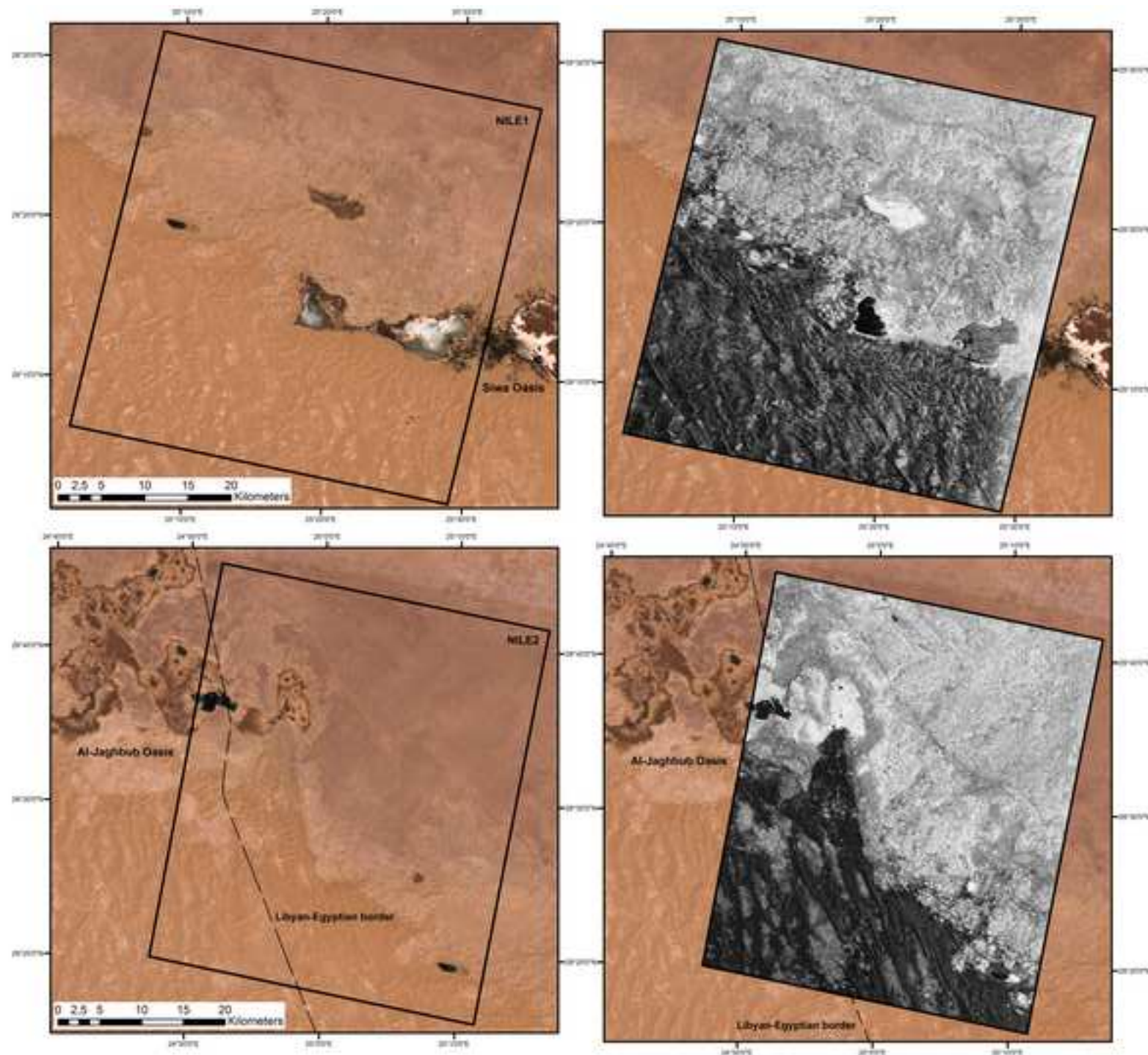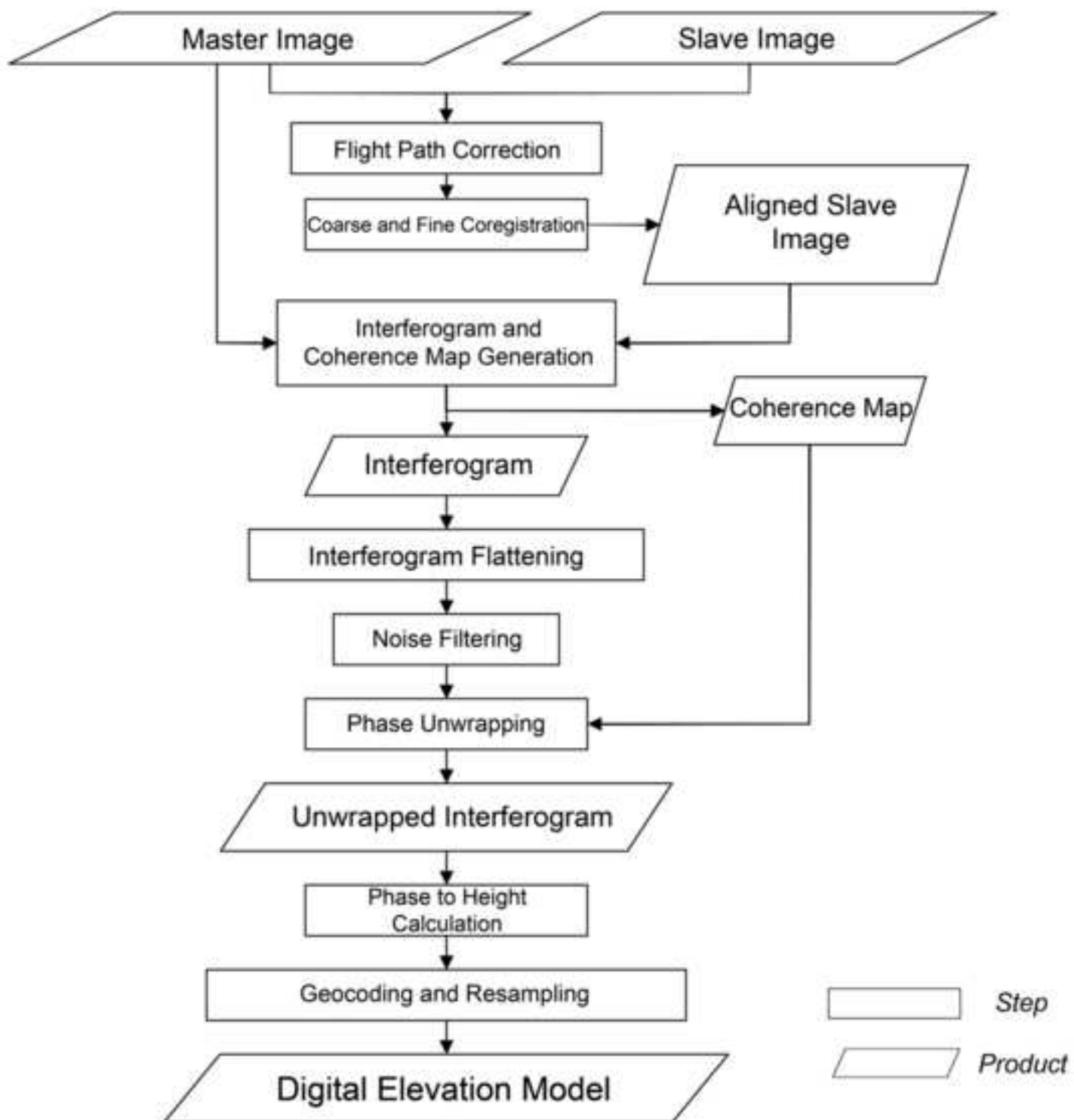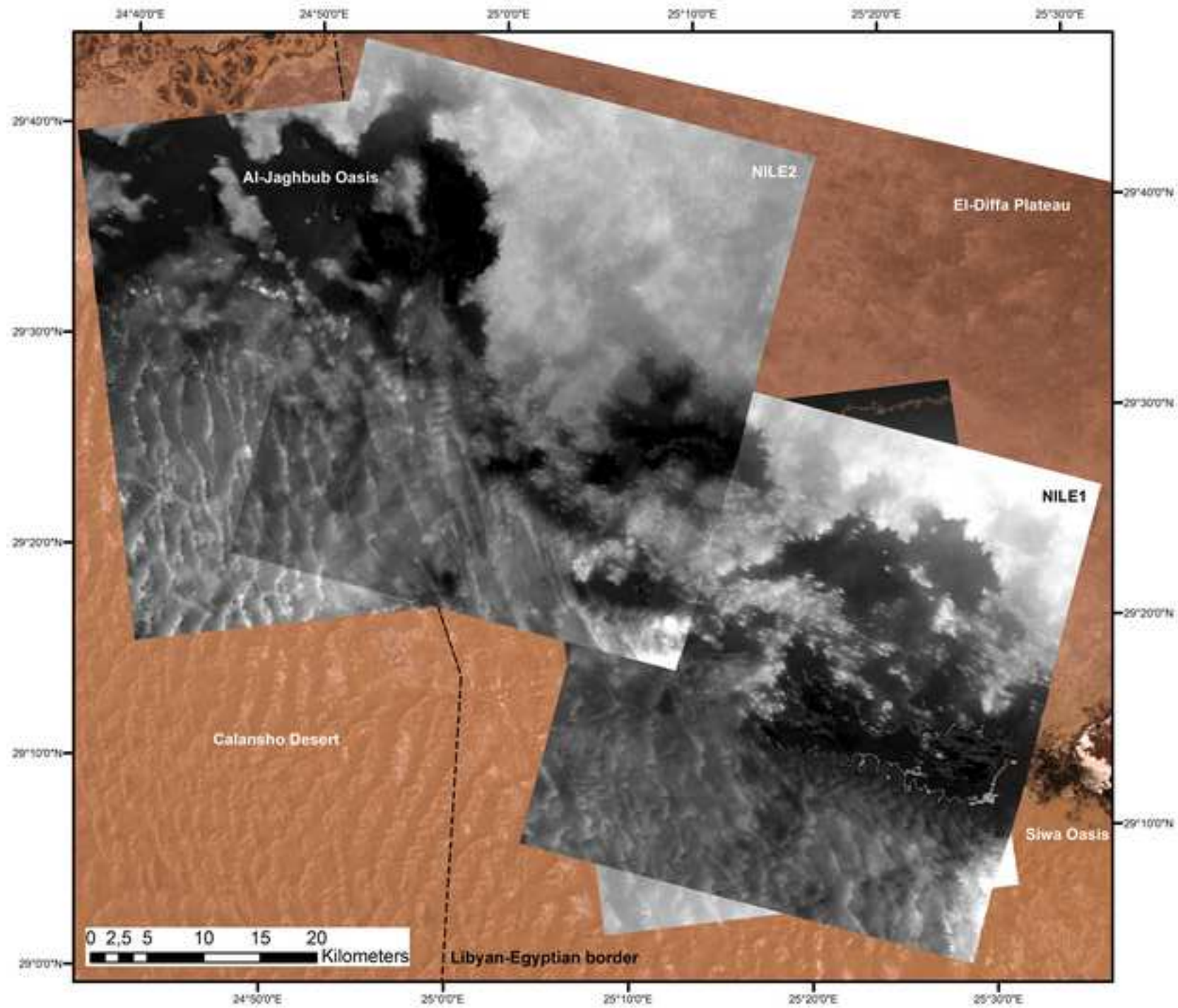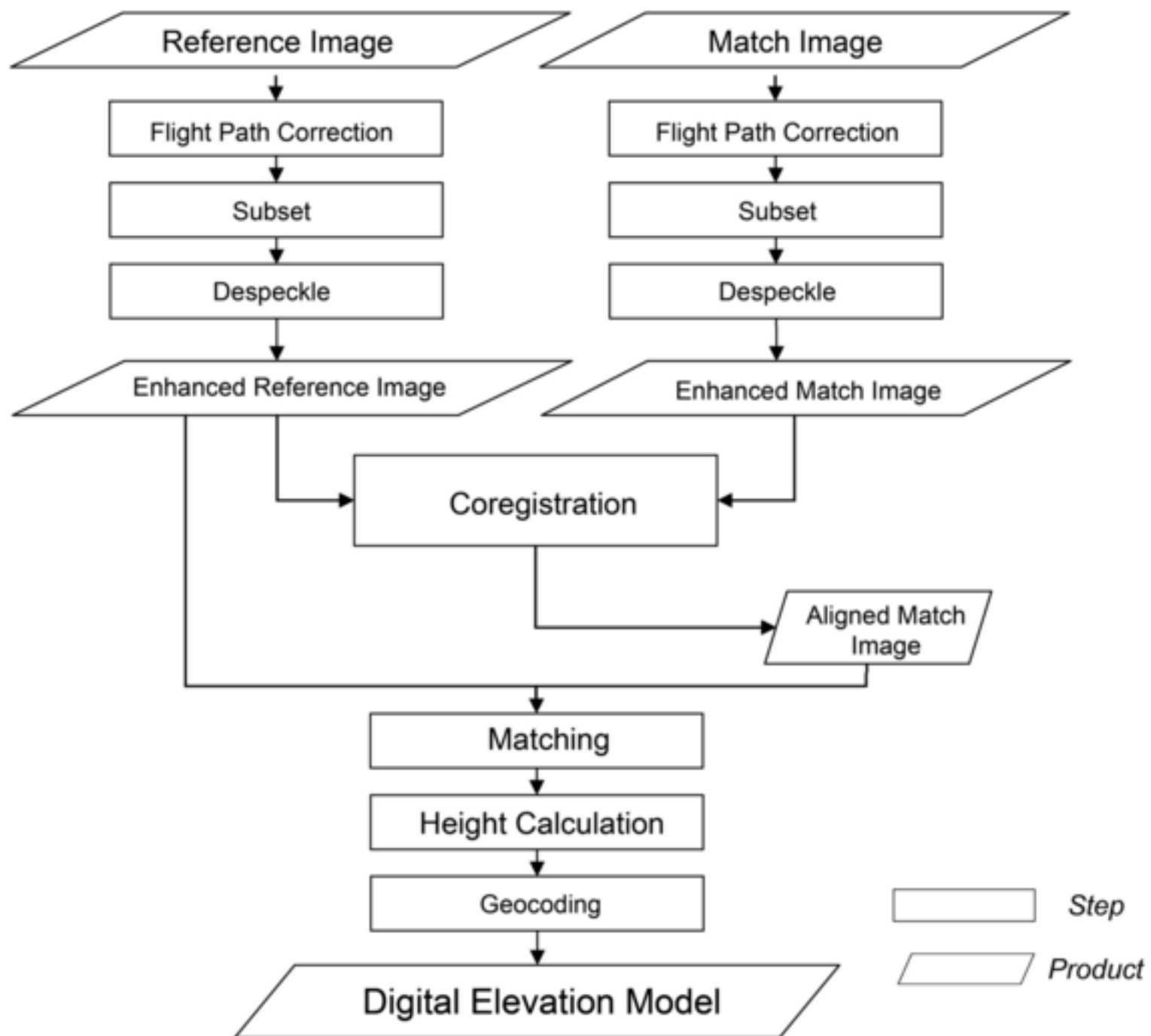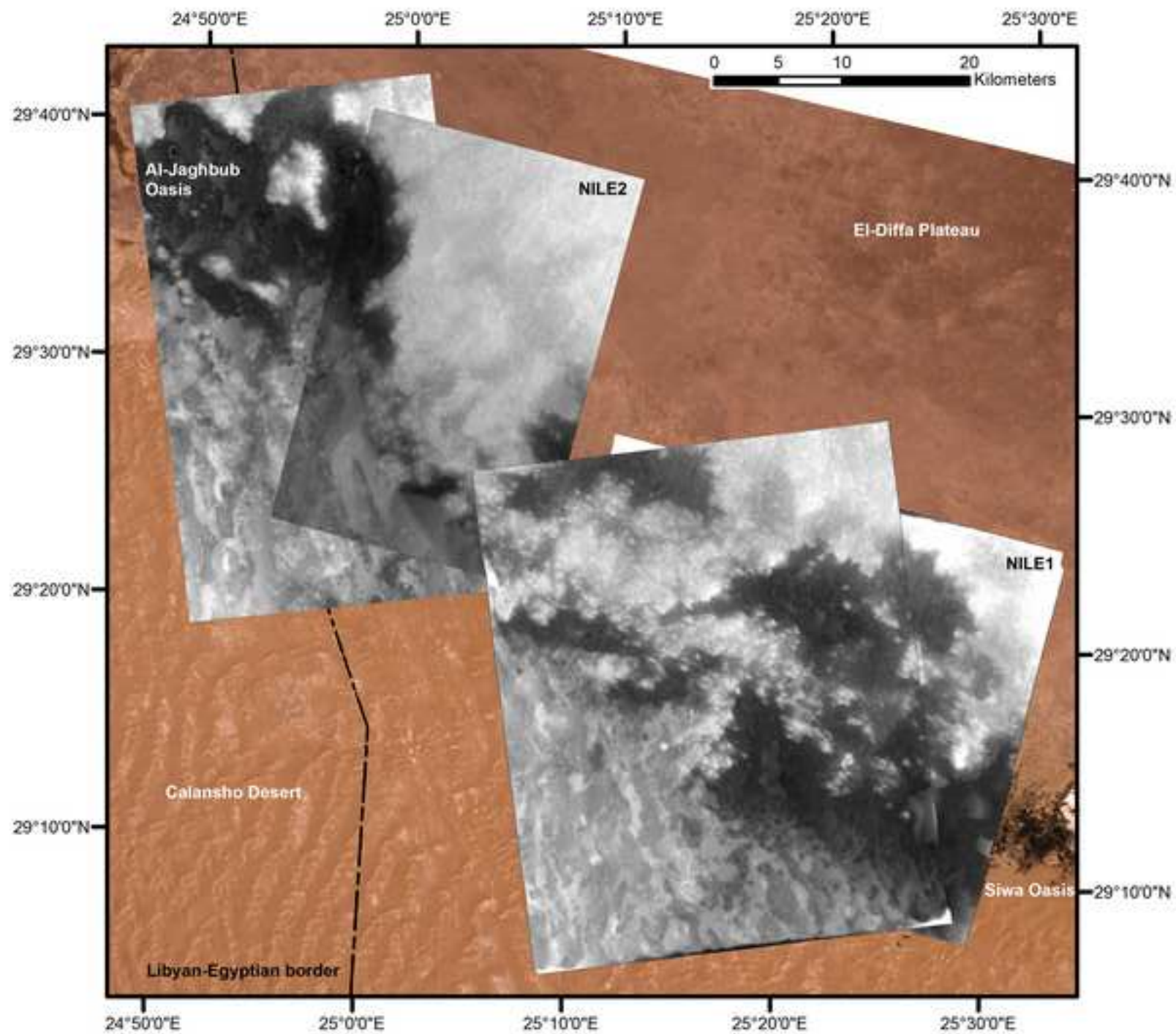
Figure 8

Figure 9

Nile 2 Descending Interferom.   Nile 2 Descending Radargramm.

Range of Residuals (m)

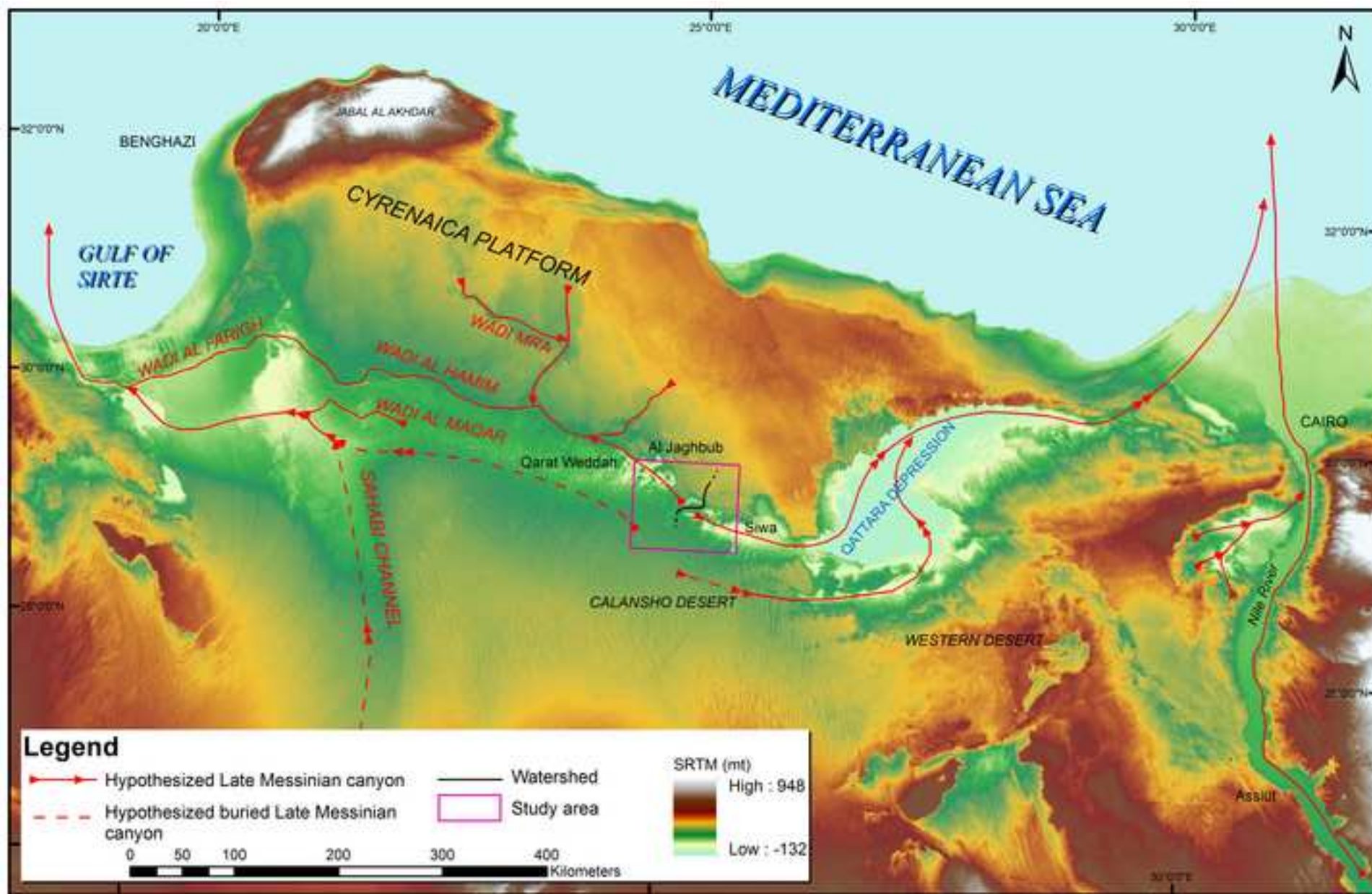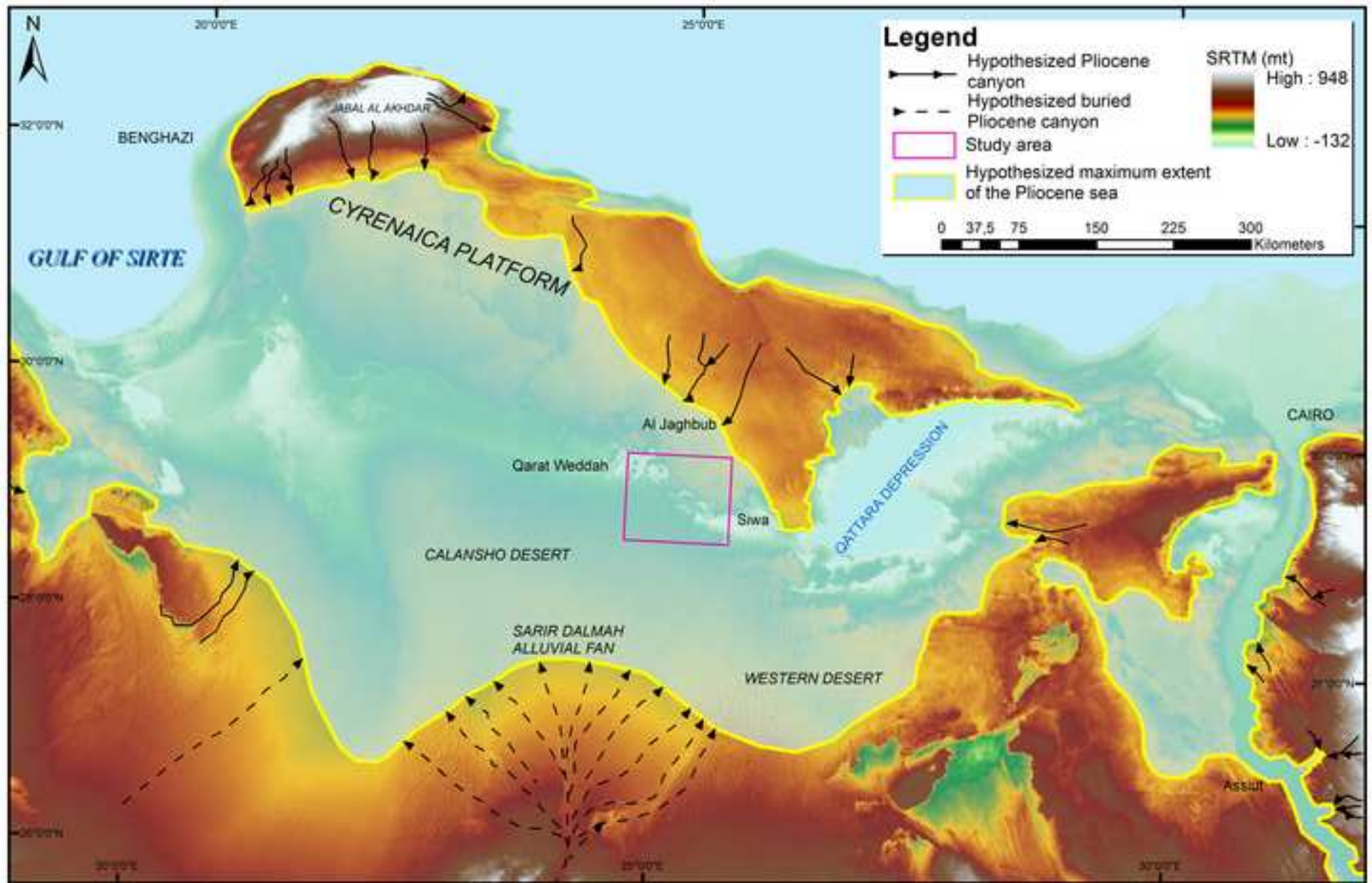|	
(grey)	Min - -40
(red)	-40 - -30
(orange)	-20 - -10
(green)	-20 - -10
(pale)	-10 - 0
(yellow)	0 - 10
(light blue)	10 - 20
(dark blue)	20 - 30
(magenta)	30 - 40
(pink)	40 - Max
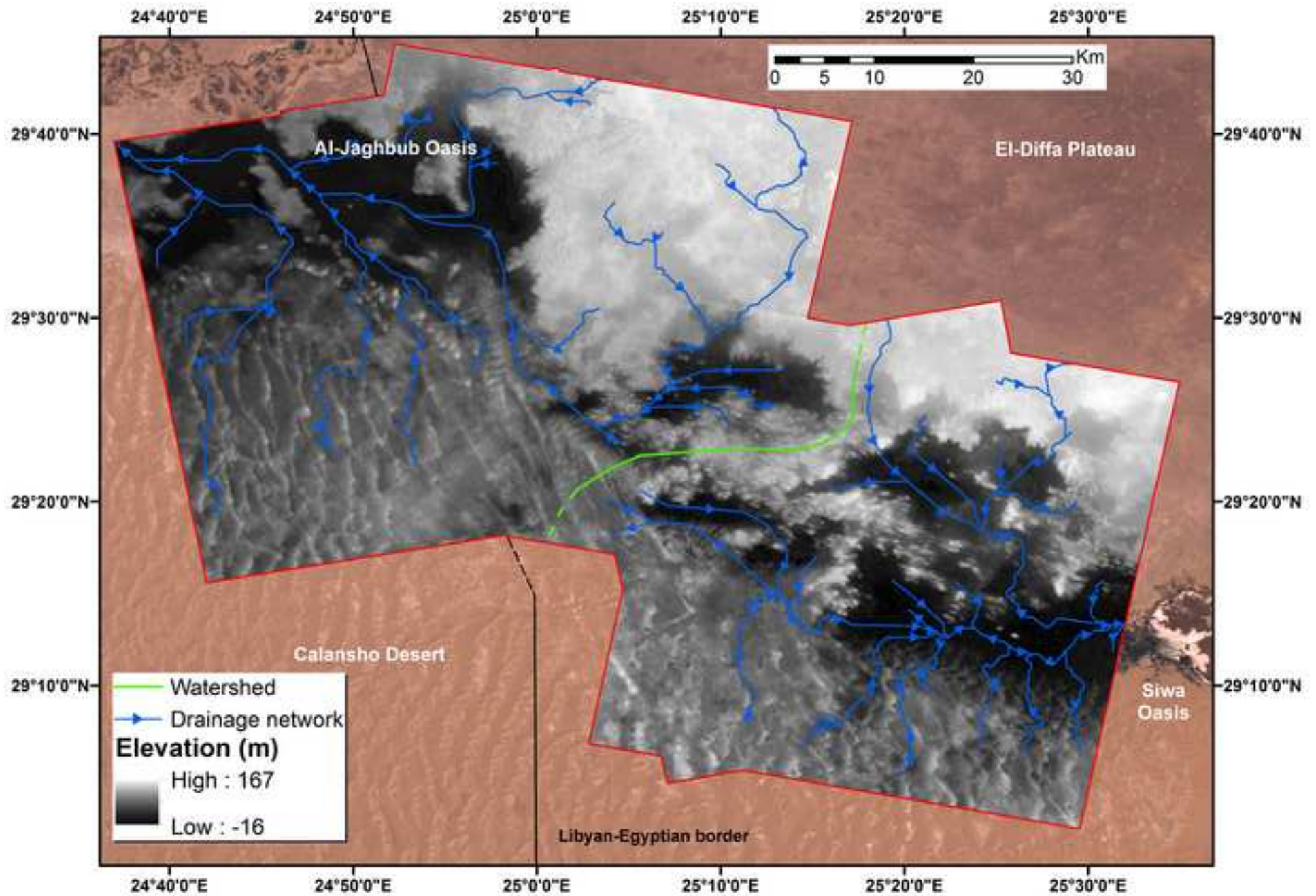
Figure 15
Click here to download high resolution image
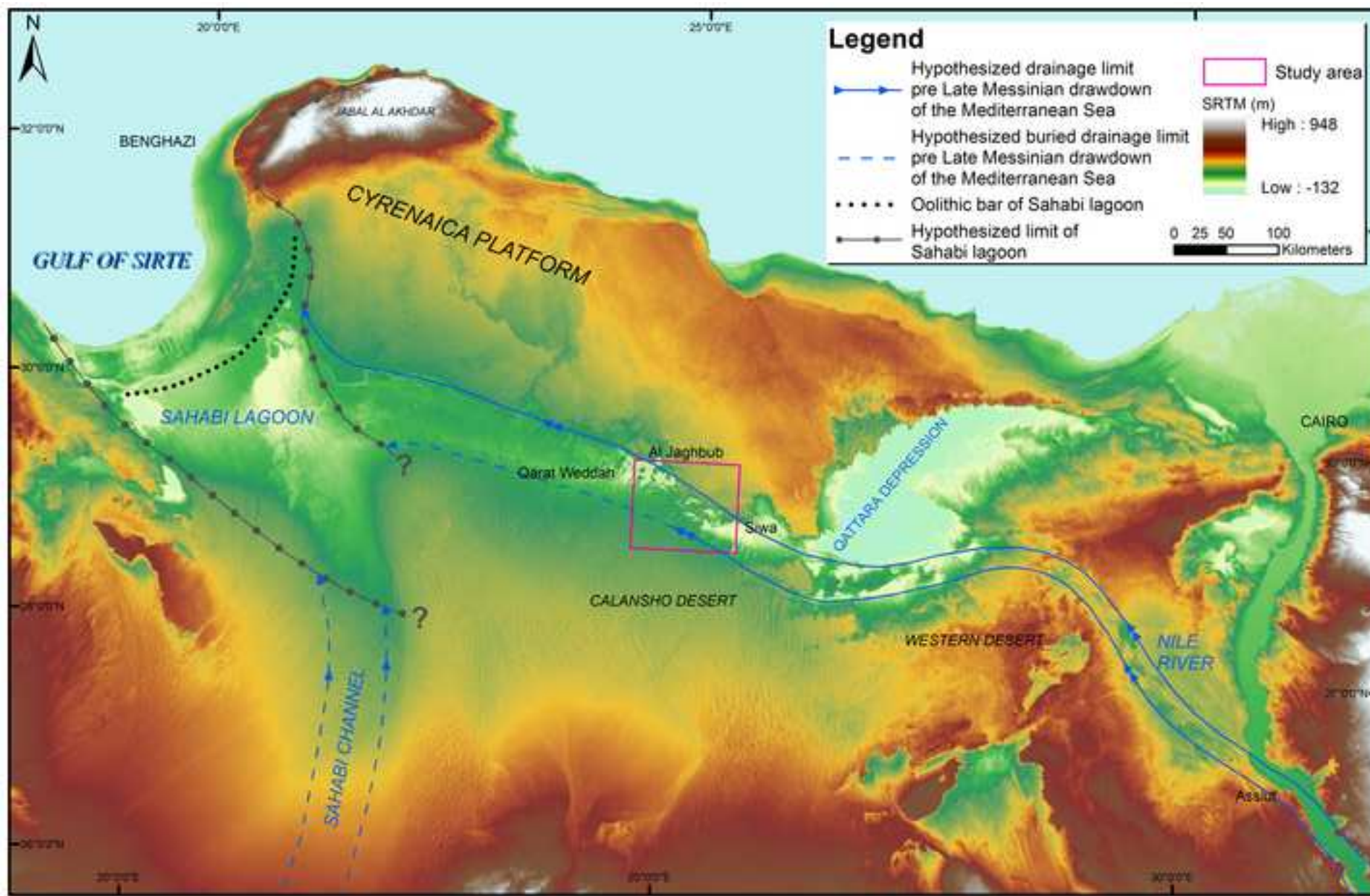
Figure 16
Click here to download high resolution image

Figure 16